scientific reports

OPEN

Mitochondrial dysfunction and increased reactive oxygen species production in *MECP2* mutant astrocytes and their impact on neurons

Danielle L. Tomasello[1], M. Inmaculada Barrasa[1], David Mankus[2], Katia I. Alarcon[3], Abigail K. R. Lytton-Jean[2], X. Shawn Liu[1,4] & Rudolf Jaenisch[1,3✉]

Studies on MECP2 function and its implications in Rett Syndrome (RTT) have traditionally centered on neurons. Here, using human embryonic stem cell (hESC) lines, we modeled MECP2 loss-of-function to explore its effects on astrocyte (AST) development and dysfunction in the brain. Ultrastructural analysis of RTT hESC-derived cerebral organoids revealed significantly smaller mitochondria compared to controls (CTRs), particularly pronounced in glia versus neurons. Employing a multiomics approach, we observed increased gene expression and accessibility of a subset of nuclear-encoded mitochondrial genes upon mutation of *MECP2* in ASTs compared to neurons. Analysis of hESC-derived ASTs showed reduced mitochondrial respiration and altered key proteins in the tricarboxylic acid cycle and electron transport chain in RTT versus CTRs. Additionally, RTT ASTs exhibited increased cytosolic amino acids under basal conditions, which were depleted upon increased energy demands. Notably, mitochondria isolated from RTT ASTs exhibited increased reactive oxygen species and influenced neuronal activity when transferred to cortical neurons. These findings underscore *MECP2* mutation's differential impact on mitochondrial and metabolic pathways in ASTs versus neurons, suggesting that dysfunctional AST mitochondria may contribute to RTT pathophysiology by affecting neuronal health.

Rett syndrome (RTT) is a devastating neurodevelopmental disorder. Classical RTT diagnosis, most commonly due to mutations in *MECP2*, is associated with severe mental disability and autism-like syndromes that manifests during early childhood. MECP2 is a pleiotropic DNA- and RNA-binding protein and multifunctional regulator of chromatin remodeling, gene expression, and other cellular pathways that remain topics of intense study[1]. This protein is expressed in all cells of the brain, yet work is still ongoing to determine the wide neurological changes due to *MECP2* LOF in RTT[2].

ASTs provide structural and molecular support for neurons that is essential for proper development and maturation[3]. Dysfunction in ASTs has been commonly observed, largely in mouse models of RTT. Mecp2 deficiency in ASTs resulted in decreased expression of glutamate transporters EAAT1/2 and increased expression of glutamine synthetase, which together resulted in a high concentrations of extracellular glutamate and excitotoxicity for neurons[4]. Increased current from GABA transporter 3 was observed in *Mecp2 KO* mouse hippocampal ASTs[5]. AST defects, including cytoskeletal atrophy, were observed in the somatosensory and motor cortex which worsened as the mice aged[6]. Adverse effects to morphology and function in neurons were observed due to AST impact and their conditioned media in both RTT mouse model and patient induced pluripotent stem cell RTT models[7–9]. Further, mouse studies have demonstrated that loss of *Mecp2* function in ASTs is sufficient to cause RTT phenotypes, and that AST-specific restoration of Mecp2 expression ameliorates these same phenotypes,

[1]Whitehead Institute for Biomedical Research, Cambridge, MA, USA. [2]Koch Institute for Integrative Cancer Research, Massachusetts Institute of Technology, Cambridge, MA, USA. [3]Department of Biology, Massachusetts Institute of Technology, Cambridge, MA, USA. [4]Present address: Department of Physiology and Cellular Biophysics, Columbia University Medical Center, New York, NY, USA. ✉email: jaenisch@wi.mit.edu

highlighting the non-cell-autonomous contribution to RTT pathophysiology[10]. What remains elusive are the molecular and biochemical changes in human ASTs due to MECP2 LOF that underlie AST dysfunction and contribute to human neuron RTT pathophysiology. We aimed to define these changes by studying hESC-derived ASTs and their interaction with neurons in a 2D and 3D context. Here, we defined the molecular mechanisms of mitochondria dysfunction through integration of metabolomic and proteomic analysis on isolated AST mitochondria. We provide novel insight into RTT pathology after we determined how dysfunctional mitochondria from RTT ASTs significantly impacts neuron function and changes to the epigenetic landscape of ASTs in hESC-derived cerebral organoids.

Results

Mitochondrial morphology defects in RTT hESC derived cerebral organoids

To elucidate the function of MECP2 in the development of the human brain, we used both female and male hESC-derived cells in 2D and 3D cultures. The WIBR3[102] is a female reporter line described in An et al.[11], with GFP or tdTomato independently inserted in frame at *MECP2* exon 3 of each X allele, resulting in early termination and a truncated LOF protein. For the second line, we generated an early stop mutation with our male hESC line to model one of the most common mutations in RTT (Supplementary Fig. 1a,b)[12]. Using CRISPR-Cas9 gene editing, linker eGFP was inserted after arginine 168 in WIBR1 hESC, resulting in early termination and a truncated LOF protein. These lines correspond to isogenic CTRs WIBR3 and WIBR1, respectively[13].

Mitochondria are critical organelles for metabolism in eukaryotes, generating both energy and precursors for biosynthesis of the essential building blocks of the cells. Beyond their metabolic roles, mitochondria are increasingly recognized as important signaling organelles, and mitochondrial dysfunction has been associated with major diseases including cancer, diabetes, and neurodegeneration[14,15]. RTT has many similarities to mitochondrial diseases, and reports from mouse models have indicated altered mitochondrial membrane potential and respiration in muscle and the brain[16]. To study the impact of MECP2 LOF on human brain development in a physiologically relevant system, we matured unguided hESC-derived neural organoids to 100 days in culture, a timepoint that matches neuronal modules at prenatal stages in vivo[17]. In order to both visualize mitochondria and differentiate cell types, we performed correlative light electron microscopy (CLEM) on the female RTT and CTR pair (WIBR3 and WIBR3[102]) (Fig. 1a,b, Supplementary Fig. 2a). Overall, we found that mitochondria from RTT organoids were significantly smaller compared to mitochondria from CTR organoids. Total area and length were decreased in RTT compared to CTR (Fig. 1c,d, Supplementary Fig. 2b,c). Separating the mitochondria based on cell type, we found a stronger phenotype in RTT glia. In addition to total area and length differences, we found increased circularity in mitochondria from RTT glia compared to CTR, suggesting a shift towards either mitochondrial fission or reduced fusion, as mitochondria are not branched and forming the same networks as CTR (Fig. 1e–g, Supplementary Fig. 2d). Measuring the total area of cristae per mitochondria, there were no statistically significant differences comparing RTT to CTR, but there was a trend for decreased cristae area in glia compared to neurons (Supplementary Fig. 2e,f). Together, this analysis indicates that RTT glia developed in a model for human brain development have altered mitochondrial morphology.

Single-nuclei multiomic analysis highlights excitatory/inhibitory imbalance in RTT cerebral organoids

MECP2 was the first methyl-binding protein discovered[18], and since then the role of MECP2 in epigenetic regulation has been studied extensively[19–23]. However, we do not fully understand the impact of *MECP2* mutations on gene expression and chromatin landscapes in the human brain, and how MECP2 functions as the brain develops. To examine both the transcriptional and epigenetic changes that occur from MECP2 LOF, we used a multiomics approach on the female RTT and CTR isogenic pair organoids at day 100 (WIBR3 and WIBR3[102]). We conducted integrated single-nuclei RNA sequencing (snRNA-seq) and Assay for Transposase-Accessible Chromatin sequencing (snATAC-seq) on RTT and CTR organoids, revealing comprehensive transcriptional and epigenetic changes. After multimodal integration, we identified 10 cell clusters on the weighted combination of gene expression and ATAC-seq peak signal multimodal neighbors (Supplementary Figs. 3a,b)[24,25]. We inferred cell type identity, cell maturation stage and anatomical semblance to the developing human cortex utilizing human and organoid datasets and references atlases[26–30] to find consensus across different developmental timepoints and high confidence in cell identity annotation. We resolved numerous glia and a heterogeneous neuron population, including early excitatory and excitatory neurons, and inhibitory interneurons (Supplementary Fig. 4a). Mapping anatomical features of the organoids by cluster, we found day 100 organoids had high semblance to human developing cortex and highlights the diversity of cells based on cluster cell type identify (Supplementary Fig. 4b).

To examine quantitative differences in cell composition, we predicted cell identity employing a singular value decomposition model built with scPred[31] trained on human cerebral cortical development by Zhu et al.[32] Single nuclei analysis was similar to cluster analysis in inferring cell types (Supplementary Figs. 4a, 5a-c). Cell composition analysis highlighted discrepancies in excitatory/inhibitory imbalance, a hallmark of RTT pathology[33], with an increase in excitatory neurons from 30% in CTR to 46% in RTT, and a decrease in inhibitory neurons from 24% in CTR to 19% in RTT (Supplementary Fig. 5d). RTT organoid composition indicated a higher density of neurons, and a lower density of radial glia, proposing increased neurogenesis directly from radial glia[34]. Gene expression profiling highlighted significant alterations in RTT ASTs and neurons, particularly affecting genes related to GABA and glutamate receptors (Supplementary Fig. 6a–e). Diving deeper into composition of our organoids, we also examined gene expression profiles of AST subtypes (Supplementary Fig. 6e). AST subtypes identified by Duran et al.[35] indicated Development group A1 had the highest total gene expression as a group in our organoids. These RTT organoids recapitulate characteristic developmental phenotypes observed as clinical features in RTT patients[36], organoids[37,38], and mouse models[39,40].
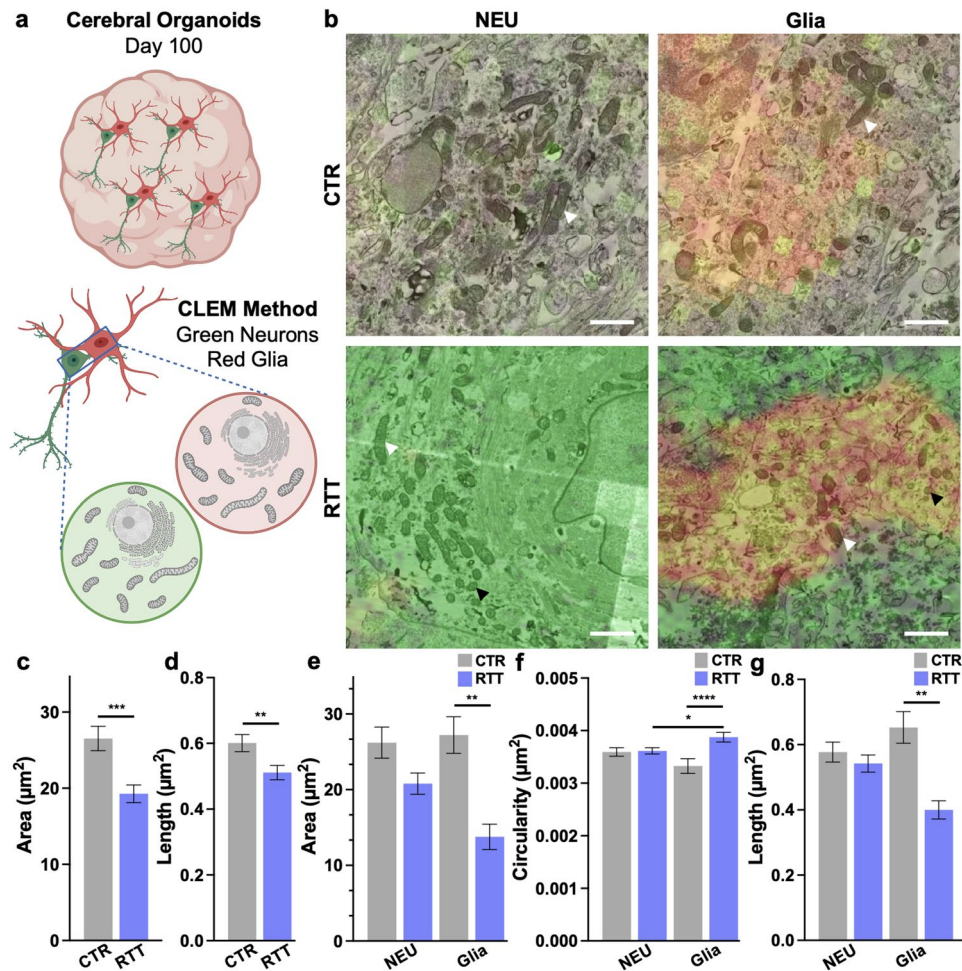
Fig. 1. Smaller, more circularized mitochondria in glia of RTT cerebral organoids. (**a**) Schematic of Correlative Light Electron Microscopy (CLEM) in matured CTR and RTT cerebral organoids. Neurons labeled in green, glia (AST/oligodendrocytes) labeled in red. (**b**) Representative images of CLEM on day 100. Left, mitochondria in neurons (NEU) (green). Right, mitochondria in glia (red). Healthy fused mitochondria (white arrowhead) and small, circular fission mitochondria (black arrowhead). Scale bar 1 µm. (**c–d**) Quantification of mitochondria ultrastructure morphology by CLEM. Significant changes in total area (**c**) and length (**d**) between CTR and RTT organoids. Statistical analysis T-Test $**p \leq 0.01$, $***p \leq 0.001$. Error bars Standard Error of Measure (SEM). (**e–g**) Significant changes in measurements comparing mitochondria in NEU and glia of RTT and CTR organoids; area (**e**), circularity (**f**), and length (**g**). Statistical analysis One-Way ANOVA with Tukey correction $*p \leq 0.05$, $**p \leq 0.01$. Total CTR n = 251, total RTT n = 430, NEU CTR n = 172, NEU RTT n = 337, Glia CTR n = 79, Glia RTT n = 93. Error bars SEM. Schematic created with BioRender.com.

Morphological and composition changes in RTT organoids

To trace transcriptional changes and examine cell morphology, we stained male and female hESC-derived organoids with neuronal and glial markers. RTT organoids showed a higher abundance of neurons compared to CTRs (Supplementary Fig. 7a). Analysis of pre- and post-synaptic markers indicated lower expression in RTT, suggesting immature neurons lacking canonical synaptic markers (Supplementary Fig. 7b). While levels of S100β and GFAP-positive ASTs were similar between RTT and CTRs, RTT ASTs exhibited altered morphology with fewer processes (Supplementary Fig. 7b). qPCR analysis at day 100 confirmed increased *RBFOX3* (NeuN) and neuronal activity marker *cFOS* transcripts in RTT organoids (Supplementary Fig. 7c), consistent with multiomic findings of increased neuronal populations (Supplementary Fig. 5d). To probe further into glial morphology, we stained cerebral organoids at a later developmental timepoint (day 200) (Supplementary Fig. 8). MOG-positive oligodendrocytes in RTT organoids displayed altered morphology compared to CTRs, while AST morphology appeared similar between groups (Supplementary Fig. 8). These results suggest immature or altered astrocyte reactivity in RTT at day 100, reflecting characteristic developmental delays. Our findings align with previous studies in human cerebral organoids showing impaired neurite growth, neurogenesis, and neural progenitor migration in RTT models[37,41–43].

Differential accessibility of genes encoding mitochondrial localized proteins in RTT ASTs that is not observed in RTT neurons

We then investigated the DNA regions that MECP2 most significantly modifies epigenetically, either directly or indirectly, in the developing human organoids. Analysis on differentially accessible peaks showed higher accessibility in RTT ASTs and neurons compared to CTR (Supplementary Fig. 9a,b). Focusing on promoter regions (2 Kb), both increased and decreased accessibility was observed in RTT compared to CTR (Supplementary Fig. 9c,d), mirroring gene expression changes (Supplementary Fig. 6a,b). Gene Set Enrichment Analysis (GSEA) of Kyoto Encyclopedia of Genes and Genomes (KEGG) metabolic pathways and Reactome gene sets revealed enrichment of amino acid metabolism and oxidative phosphorylation (OxPhos) pathways in RTT ASTs and neurons compared to CTR (Fig. 2a,b; Supplementary Fig. 10a,b), with additional enrichment in glycolysis and mitochondrial translation in neurons (Fig. 2b; Supplementary Fig. 10b). Ranking by promoter accessibility showed more significant enrichment, particularly in ASTs (Fig. 2c,d; Supplementary Fig. 10c,d).

Examining nuclear-encoded mitochondrial genes[44], significant differential promoter accessibility was more pronounced in RTT neurons than RTT ASTs compared to CTRs (Fig. 2e–h). We then investigated the cell type-specific impact due to mutation of *MECP2*. Comparing gene expression between neurons and ASTs in RTT and CTR, we observed differences in metabolic pathways, particularly in ASTs (Fig. 3a–b). However, when we examined accessibility of mitochondrial genes, there were small changes in CTR ASTs compared to CTR neurons (Fig. 3c), but abundant changes in accessibility in RTT ASTs compared to RTT neurons (Fig. 3d-f). Further, examining gene ontology of differentially accessible promoter regions that do not overlap between CTR and RTT conditions, we found the majority of genes with increased promoter accessibility are involved in metabolism (Fig. 3c–f). From this data, we postulate that mutation of *MECP2* in ASTs differentially impacts accessibility of a group of mitochondrial genes as compared to neurons.

Characterization of RTT hESC-derived ASTs

We went on to study how mutation of *MECP2* differentially impacts AST metabolism and function. Differentiation of hESC lines to mature ASTs in 2D was confirmed with expression of AST markers NDRG2, GFAP and EAAT2 (Supplementary Fig. 11). AST reactivity is a response to pathological conditions or perturbations in cellular homeostasis, with enlargement in the cell body and processes (hypertrophy), and altered levels of transcripts and proteins[45]. To assess human AST reactivity in our genetic models for RTT, we followed the guidelines from Escartin et al.[46]. We used multiple markers and factors to examine ASTs that were defined in a pathological context from multiple human diseases. We first tested a panel of compiled reactivity markers by quantitative PCR (qPCR) (Fig. 4a). Similar to reactive changes observed in disease pathology[46], RTT ASTs had increased relative levels of transcripts involved in metabolism (*TSPO*) and intermediate filaments (*GFAP*). Mitochondrial encoded NADH dehydrogenase 5 (*MT-ND5*) was the most significantly upregulated gene (Fig. 4a). ASTs were then seeded at a low density to examine cytoskeletal reorganization (Supplementary Fig. 12). Measuring dimensions of the cell cytoskeleton with β-actin, we found that RTT AST have a smaller surface area compared to CTR ASTs (Supplementary Fig. 13a). Quantifying mitochondria with mitochondrial import receptor subunit TOM20 indicated similar morphological defects to mitochondria as RTT cerebral organoids (Fig. 1). TOM20 showed a lower abundance of mitochondria with fewer branches and branch end points in RTT ASTs compared to CTR (Fig. 4b, Supplementary Fig. 13b). Together, RTT ASTs showed hallmarks of altered reactivity and function similar to other disease pathologies[46].

We assessed mitochondrial parameters using MitoTracker Deep Red to measure mitochondrial mass and MitoSOX to quantify superoxide production, a byproduct of OxPhos and reactive oxygen species (ROS) production (Fig. 4c–e). Our results revealed a significant decrease in total MitoTracker fluorescence per cell in RTT ASTs, indicating reduced mitochondrial mass compared to CTR (Fig. 4c, Supplementary Fig. 13c), although there was no difference in MitoTracker intensity per mitochondrion (Fig. 4d). Surprisingly, despite lower mitochondrial abundance, RTT ASTs exhibited similar levels of superoxide production compared to CTR ASTs under basal conditions (Fig. 4e).

Glutamate (GLU) is a neurotransmitter and also an essential energy source in the brain that feeds into the mitochondrial tricarboxylic acid (TCA) cycle, or is amidated to glutamine and released from ASTs for neuronal uptake[47]. Upon GLU treatment (200 μM), both RTT and CTR ASTs showed a decrease in MitoTracker fluorescence (Fig. 4c,d). This GLU-induced effect aligns with findings by Azarias et al.[48], suggesting GLU-induced intracellular acidification in ASTs influences mitochondrial function and reduces ROS production. Interestingly, after GLU exposure, RTT ASTs displayed significantly higher levels of MitoSOX fluorescence compared to CTR, indicating elevated ROS production despite reduced mitochondrial mass (Fig. 4e). We additionally performed a functional test for GLU clearance, a critical role for ASTs at the excitatory synaptic cleft. Okabe et al. have previously identified diminished GLU clearance in cultured mouse Mecp2-deficient ASTs[4], and Sun et al.[49] found decreased GLU clearance in MECP2 R270X hESC-derived ASTs. Similarly, we found diminished GLU clearance in human RTT ASTs compared to CTR (Supplementary Fig. 13c). These findings indicate RTT ASTs have decreased mitochondrial mass and similar levels of ROS under basal conditions. After incubation with GLU, RTT ASTs show higher levels of ROS compared to CTR, underscoring the complex interplay between GLU metabolism, mitochondrial dynamics, and oxidative stress in RTT ASTs.

We went on to examine mitochondrial and glycolytic function by Seahorse assay. Overall, oxygen consumption rate (OCR) was significantly lower in RTT ASTs, with OCR levels for basal, adenosine triphosphate (ATP)-linked, and maximal respiration significantly lower than CTR OCR levels (Fig. 5a). The presentation of the mitochondrial phenotype occurs once the glial progenitor cells mature to ASTs, shifting from glycolytic metabolism (Supplementary Fig. 13d). Examining glycolytic extracellular acidification rates (ECAR), we found no significant differences between RTT and CTR ASTs (Fig. 5b). Altered bioenergetics in RTT ASTs was further
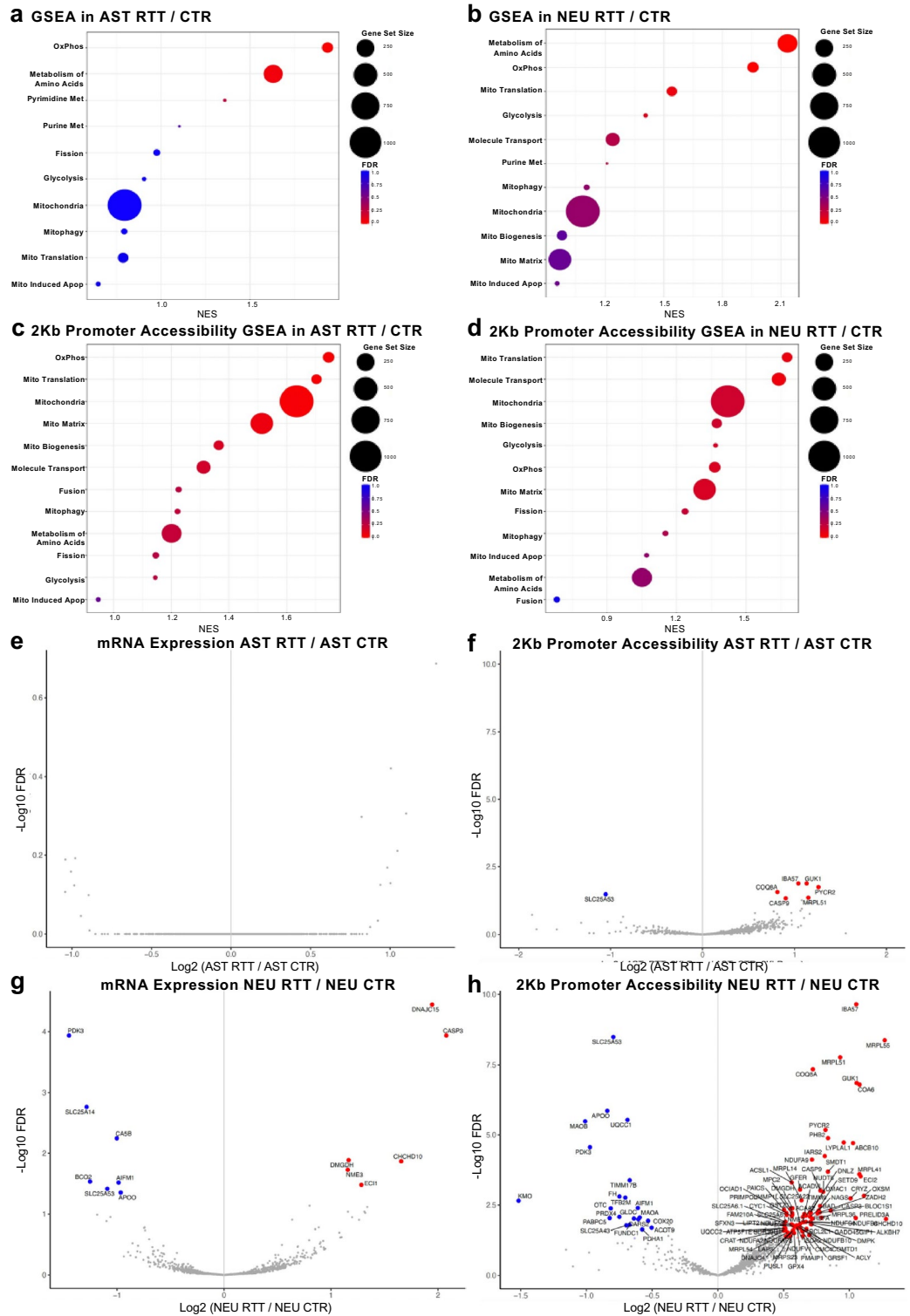
Fig. 2. Promoter regions of RTT ASTs and NEUs more significantly accessible compared to gene expression. (**a–d**) Dot plots of gene set enrichment analysis (GSEA) of mitochondrial and metabolic pathways of interest. **a-b**) Genes ranked by expression fold change. (**a**) ASTs of RTT compared to CTR. FDR ≤ 0.25 oxidative phosphorylation (OxPhos) and metabolism of amino acids. (**b**) NEUs of RTT compared to CTR. FDR ≤ 0.25 metabolism of amino acids, OxPhos, mitochondrial translation, glycolysis, and molecule transport. (**c–d**) Genes ranked by 2 Kb promoter accessibility fold change. (**c**) ASTs of RTT compared to CTR. FDR ≤ 0.25 OxPhos, mitochondrial translation, mitochondria proteome, mitochondrial matrix, mitochondrial biogenesis, mitochondrial molecule transport, mitophagy, and metabolism of amino acids. (**d**) NEUs of RTT compared to CTR. FDR ≤ 0.25 mitochondrial translation, mitochondrial molecule transport, mitochondria proteome, mitochondrial biogenesis, glycolysis, oxidative phosphorylation, mitochondrial matrix, and fission. (**e–h**) Analysis of nuclear-encoded mitochondrial genes as identified by MitoCarta3.0[44]. (**e**) Volcano plot of differential gene expression in ASTs of RTT compared to CTR. (**f**) Volcano plot of differential accessibility of 2 Kb promoter-linked genes in ASTs of RTT compared to CTR. (**g**) Volcano plot of differential gene expression in NEUs of RTT compared to CTR. (**h**) Volcano plot of differential accessibility of 2 Kb promoter-linked genes in NEUs of RTT compared to CTR. Significantly increased transcripts in red, significantly decreased transcripts in blue. Adjusted $p \leq 0.05$.
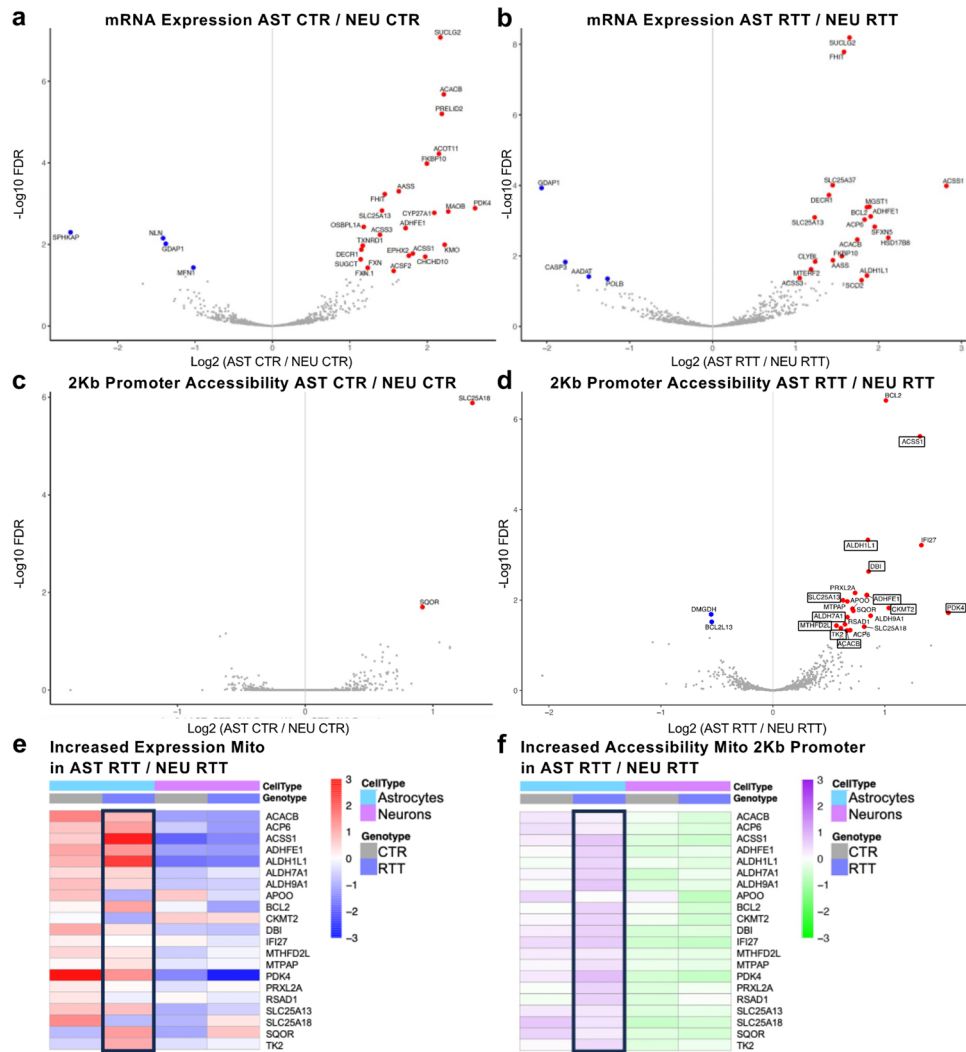
Fig. 3. Cell type specific changes in promoter regions of nuclear-encoded mitochondrial genes in RTT ASTs. (**a–d**) Analysis of nuclear-encoded mitochondrial genes (mitochondria proteome) as identified by MitoCarta3.0[44]. (**a**) Volcano plot of differential gene expression changes in CTR ASTs compared to CTR NEUs. (**b**) Volcano plot of differential gene expression changes in RTT ASTs compared to RTT NEUs. (**c**) Volcano plot of differential accessibility changes of 2 Kb promoter-linked genes in CTR ASTs compared to CTR NEUs. (**d**) Volcano plot of differential accessibility changes of 2 Kb promoter-linked genes in RTT ASTs compared to RTT NEUs. Significantly increased transcripts in red, significantly decreased transcripts in blue. Boxes; 2 Kb promoter-linked genes with metabolic activity that do not overlap with significantly altered 2 Kb promoter-linked genes in CTR ASTs compared to CTR NEUs. Adjusted $p \le 0.05$. (**e**) Heat map of increased accessible genes in red from (**d**) with CTR and RTT ASTs and NEUs. (**f**) Heat map of 2 Kb promoter-linked genes of increased accessible genes in red from (**d**) with CTR and RTT ASTs and NEUs.

exemplified by decreased total ATP levels (Supplementary Fig. 13e). Together, RTT ASTs show significant defects in mitochondrial function that impacts their overall ATP levels.

Integration of proteomic and metabolomic profiles uncovers mechanism of mitochondrial dysfunction

Recently, studies have identified biomarkers that correlate with metabolic dysfunction in autism spectrum disorders (ASD)[50,51]. What is not well characterized in the neurodevelopment field are the metabolic changes at the cellular level in the brain, specifically how altered metabolites impact cell function and maturation. We asked if there was a connection between altered metabolism and RTT, and examined potential biochemical and molecular differences between RTT and CTR ASTs with whole-cell metabolite and proteomic profiling. Whole-cell polar metabolomic analysis identified significant changes in metabolite abundances in glycerophospholipid metabolism (increased phosphocholine), glycolysis (increased lactate) and pentose phosphate pathway (decreased UDP-hexose), and pyrimidine metabolism (decreased carbamoyl aspartate) in RTT ASTs compared to CTR
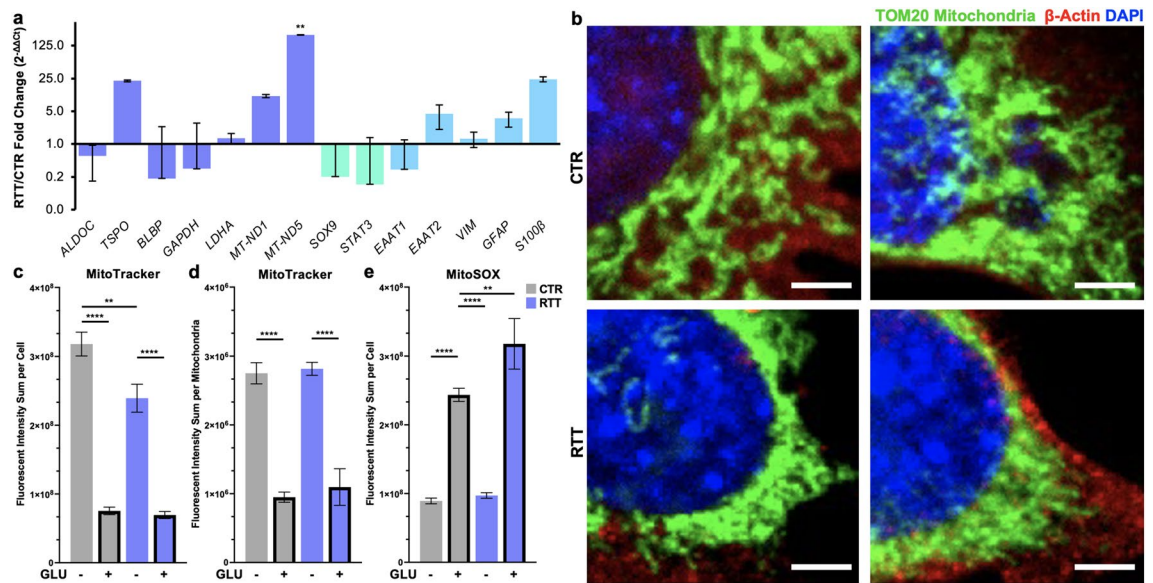
Fig. 4. Human RTT AST characterization and function. (**a**) Quantitative PCR panel of AST reactive markers[46]. Marker colors: energy metabolism and mitochondria (purple), transcription factors (green), and AST (blue) markers in RTT compared to CTR. Transcripts normalized to 18S. CTR n = 8, RTT n = 8, performed in triplicate per value. Statistical analysis Two-Way ANOVA with Bonferroni correction **$p \leq 0.01$. Error bars (SEM). (**b**) Representative images of CTR (top panel) and RTT (bottom panel) ASTs for reactivity and mitochondrial morphology imaging. Mitochondria (TOM20), Actin cytoskeleton (β-Actin). Merge with DAPI. Scale bar 5 μm. (**c–e**) Quantification of MitoTracker or MitoSOX in the absence (− GLU) or presence (+ GLU) of 200 μM glutamate (GLU) for 24 h. (**c**) MitoTracker fluorescence per cell. Images for quantification Media CTR n = 32, RTT = 32, + GLU CTR n = 32, + GLU RTT n = 17. (**d**) MitoTracker fluorescence per mitochondria. Media CTR n = 32, RTT = 32, + GLU CTR n = 31, + GLU RTT n = 16. (**e**) MitoSOX fluorescence per cell. Media CTR n = 32, RTT = 32, + GLU CTR n = 17, RTT n = 17. Statistical analysis Two-Way ANOVA with Bonferroni correction **$p \leq 0.01$, ****$p \leq 0.0001$. Error bars SEM.

(Table 1). Notably, an abundance of numerous amino acids was significantly increased, including arginine, lysine, methionine, proline, threonine, and tryptophan. Through transamination or deamination reactions, amino acids can be converted into intermediates of TCA cycle (Fig. 5c).

Performing whole cell proteomic analysis, we focused on proteins involved in metabolism and mitochondrial function. We found amino acid metabolism (Fig. 5d), glycolysis/gluconeogenesis (Fig. 5e), and mitochondrial proteins (Fig. 5f) significantly impacted. Among altered mitochondrial proteins, we observed a large decrease in protein abundances in OxPhos Complex I (NDUFS2, NDUS4, NDUS6, NDUV4), and ATP synthase Complex V (ATPD, ATPG) (Fig. 5f). With the decreased mitochondrial abundance in RTT ASTs, we thought it imperative to examine the metabolomic and proteomic profile of mitochondria in isolation. Fractionation of mitochondria was confirmed by western blot analysis, with mitochondrial import protein TOM20 found in the mitochondrial fraction and not cytosolic (Supplementary Fig. 14). By proteomic analysis, we indeed found small but significantly altered protein abundances similar to those resolved by whole cell proteomics (Figs. 5f, 6a). Performing gene ontology analysis, we found the majority of altered proteins to function in metabolism, and a large abundance of significantly decreased proteins within the electron transport chain (ETC) and ATP synthesis, including Complex I (NDUFA9, NDUFA10, NDUFB10, NDUFC2, NDUFS8), Complex III (QCR1, QCR2, QCR10), and Complex V (ATP5E1, ATPF1, ATP5G1) (Fig. 6a,b). We then probed the metabolome of the isolated mitochondria. We resolved similar metabolites compared to previously published human MITObolome[52]. Contrary to the whole cell RTT metabolome, we discovered diminished abundance of many amino acids (histidine, glutamate, methionine, phenylalanine, proline, threonine), metabolites involved in cofactor/redox metabolism (1-methylnicotinamide and nicotinamide), nucleotide metabolism (adenosine, ADP, IMP, UDP-GlcNAc), and intermediates of the TCA Cycle (citrate and malate) in RTT compared to CTR mitochondria (Table 2). We then integrated the mitochondrial proteomic and metabolomic analyses, and found altered protein abundances correlate to perturbations in metabolites, with amino acid metabolism converging around the TCA cycle (Fig. 6c). Within the TCA cycle, Aconitase (ACON) was decreased, a protein that catalyzes isomerization of citrate to isocitrate. We found an increased abundance of malate carrier protein M2OM aligns with decreased malate in the mitochondria. Together, we defined biochemical evidence tied to mitochondrial metabolic and energetic dysfunction after *MECP2* LOF in RTT ASTs.

RTT ASTs rely on amino acid catabolism as compensatory mechanism for diminished energetics

To test how RTT ASTs adapt to environmental changes, we probed the response to metabolic shift after changing the carbon source in the media. We tested how RTT ASTs accommodate changes to energy metabolism with
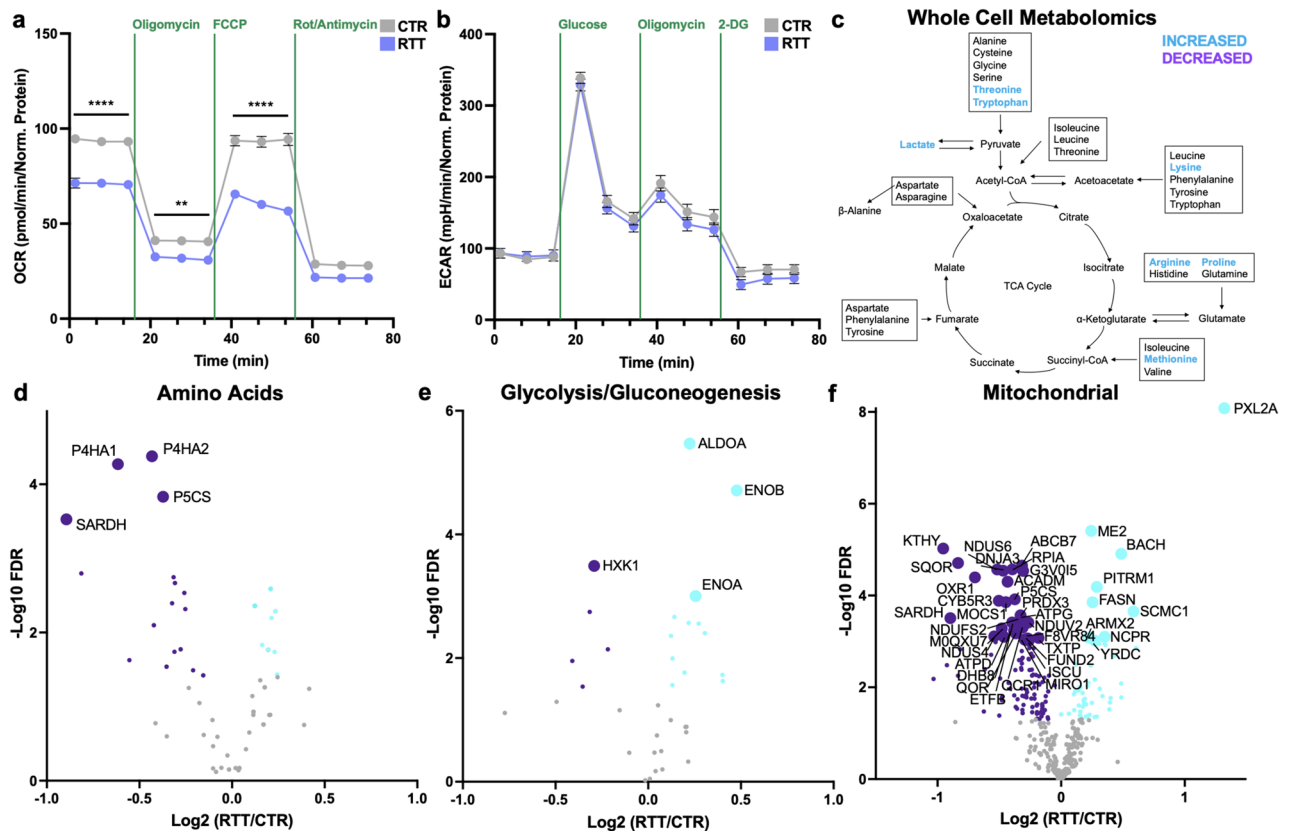
Fig. 5. Dysfunctional mitochondrial respiration and increased amino acids in RTT ASTs. (**a**) Mitochondria stress test of CTR and RTT ASTs. To evaluate mitochondrial function, cells were injected with oligomycin (Complex V Inhibitor), carbonyl cyanide-4-(trifluoromethoxy)phenylhydrazone (FCCP, collapses proton gradient), and rotenone/antimycin A (Complex I and Complex III Inhibitors). CTR n = 91, RTT n = 91, Statistical analysis Two-Way ANOVA with Bonferroni correction $**p \leq 0.01$, $****p \leq 0.0001$. Error bars SEM. (**b**) Glycolysis stress test of CTR and RTT ASTs. Glycolysis was increased with glucose and oligomycin injection, followed by blocking of glycolysis with competitive glucose analog 2-DG. CTR n = 45, RTT n = 44. Statistical analysis Two-Way ANOVA with Bonferroni correction. Error bars SEM. (**c**) Whole cell AST metabolomics summary. TCA cycle with metabolite changes of RTT relative to CTR (significantly increased in blue). CTR n = 9, RTT n = 10. Full metabolite changes in Table 1. (**d**–**f**) Volcano plots of whole cell AST proteomic analysis of pathways of interest. Total protein (UniProt) changes of RTT compared to CTR, protein changes in amino acids (**d**) glycolysis/gluconeogenesis (**e**), and mitochondrial proteins (**f**). Significantly increased proteins (light blue), significantly decreased proteins (purple) in RTT compared to CTR. Large dots labeled with adjusted $***p \leq 0.001$, small dots adjusted $*p \leq 0.05$. CTR n = 6, RTT n = 6.

the following three media conditions. *One*, glucose in media was exchanged for galactose (GAL). Cells cultured in galactose are unable to generate sufficient ATP from glycolysis, increasing mitochondrial OxPhos for ATP generation, and consequently are more sensitive to mitochondrial perturbation than cells grown in glucose[53–56]. *Two*, glucose in media was exchanged for lipid cocktail (LIP). Fatty acid β-oxidation is a pathway which occurs in mitochondria to produce energy from lipids[57]. *Three*, pyruvate was removed from the media (-PYR), which disrupts the glycolysis–TCA cycle flux[58]. We performed whole cell metabolomics on ASTs after incubation with the above conditions for 24 h (Table 3). Overall, we found minimal changes to metabolites in CTR AST. GAL and LIP conditions in CTR ASTs depleted levels of lactate and increased levels of aspartate, while -PYR condition in CTR ASTs depleted ATP levels compared to glucose media (Fig. 7a,b, Table 3). When we examined the RTT ASTs, we found a large shift in metabolites in all conditions compared to glucose media. We observed similar changes compared to the shift in CTR AST metabolites, however, there was a significant decrease in a staggering number of metabolites overall. This includes metabolites in the pentose phosphate pathway (UDP-hexose GAL, LIP) and pyrimidine metabolism (beta-alanine GAL, LIP, -PYR) and TCA Cycle (citrate GAL, LIP, -PYR, malate GAL) that were not observed in CTR ASTs. Of particular interest, we identified decreased abundance of metabolites in all amino acid metabolism pathways (Fig. 7a,b, Table 3). Significantly lower amino acid abundances were similar between all three conditions in RTT ASTs compared to glucose media levels. We propose RTT ASTs accommodate prolonged stress from changes in energy metabolism and demand by catabolism of amino acids.

Exogenous mitochondria can minimize RTT AST mitochondrial stress similar to ROS scavenger

The exchange of mitochondria and recycling of damaged mitochondria is an essential function between cells in the brain[59]. Multiple mechanisms have been identified for transcellular mitochondrial movement, including

Whole Cell Metabolomics	Metabolite	CTR Mean	CTR SEM	RTT Mean	RTT SEM	RTT/CTR p-value
Acetyl Group	acetylcarnitine	3.47E-02	0.01	2.55E-02	0.01	
	acetylserine	1.44E-01	0.02	1.78E-01	0.01	
	butyryl carnitine	1.11E-04	0.00	1.00E-04	0.00	
	C5-carnitines	5.56E-04	0.00	1.60E-03	0.00	
	carnitine	6.67E-04	0.00	1.00E-04	0.00	
	GSH	3.34E+00	0.54	4.63E+00	0.63	***
	N-acetylglutamate	8.22E-03	0.00	4.96E-02	0.02	
	propionylcarnitine	1.44E-03	0.00	1.40E-03	0.00	
Ala Asp Glu	alanine	7.54E+00	1.28	2.06E+01	5.49	
	asparagine	1.57E-01	0.05	4.49E-01	0.13	
	aspartate	1.30E+01	2.43	9.53E+00	1.49	
	glutamate	4.27E+01	2.97	4.13E+01	3.91	
	glutamine	1.77E+01	2.38	2.78E+01	7.10	
Arg Biosynthesis	arginine	2.02E+01	2.34	3.79E+01	10.53	**
	argininosuccinate	7.94E-02	0.02	2.98E-01	0.11	
	citrulline	1.38E-02	0.00	1.84E-02	0.01	
	N-acetylglutamate	8.22E-03	0.00	4.96E-02	0.02	
	Na-acetylornithine	1.67E-03	0.00	5.00E-04	0.00	
	ornithine	2.22E-04	0.00	1.00E-04	0.00	
Arg Pro	asparagine	1.57E-01	0.05	4.49E-01	0.13	
	creatine	5.33E-03	0.00	4.27E-01	0.19	
	hydroxyproline	1.49E-02	0.00	1.92E-02	0.00	
	phosphocreatine	0.00E+00	0.00	1.07E-01	0.04	
	proline	6.09E+01	15.22	1.26E+02	17.75	****
Cofactor/Redox Balance	1-methylnicotinamide	9.60E+01	16.83	8.77E+01	16.44	
	acetyl-CoA	6.78E-03	0.00	3.19E-02	0.00	
	alpha-lipoic acid	0.00E+00	0.00	0.00E+00	0.00	
	FAD	0.00E+00	0.00	0.00E+00	0.00	
	GSH	3.34E+00	0.54	4.63E+00	0.63	
	GSSG	2.44E+00	0.30	3.48E+00	0.71	
	NAD	2.41E+00	0.36	3.69E+00	0.39	
	NADH	2.29E-02	0.01	2.70E-02	0.00	
	NADP	6.20E-02	0.02	6.85E-02	0.01	
	NADPH	1.30E-01	0.02	1.81E-01	0.01	
	nicotinamide	2.18E+00	0.24	4.42E+00	1.34	
	nicotinic acid	4.44E-04	0.00	5.00E-04	0.00	
	pantothenic acid	1.66E+01	1.76	2.91E+01	4.98	
	S-adenosylmethionine	1.52E+00	0.21	3.05E+00	0.43	
Cys Met	cystathionine	2.22E-04	0.00	1.80E-03	0.00	
	cystine	1.78E-03	0.00	2.23E-02	0.01	
	GSH	3.34E+00	0.54	4.63E+00	0.63	
	methionine	6.12E+00	0.60	1.11E+01	3.15	**
	S-adenosylhomocysteine	3.71E-02	0.01	7.40E-02	0.02	
	S-adenosylmethionine	1.52E+00	0.21	3.05E+00	0.43	
Fatty Acid Synthesis	acetylcarnitine	3.47E-02	0.01	2.55E-02	0.01	
	palmitate	4.06E-02	0.02	1.15E-02	0.00	
Glycerophospholipid	choline	8.54E+01	31.37	9.34E+01	15.86	
	glycerol 3-phosphate	1.03E-01	0.03	5.29E-02	0.01	
	glycerophosphocholine	2.04E+01	3.47	3.22E+01	2.62	
	phosphocholine	4.43E+02	61.95	7.01E+02	75.39	****
	phosphoethanolamine	6.54E-01	0.22	7.94E-02	0.01	
Gly Ser Thr	acetylserine	1.44E-01	0.02	1.78E-01	0.01	
	betaine	1.08E-01	0.08	0.00E+00	0.00	
	glycine	1.41E+00	0.15	1.60E+00	0.31	
	guanidinoacetate	0.00E+00	0.00	0.00E+00	0.00	
	phosphoserine	4.31E-02	0.01	1.79E-02	0.01	
	sarcosine	9.89E-03	0.01	1.89E-02	0.01	
	serine	1.14E+00	0.11	2.48E+00	0.82	
	threonine	3.70E+01	2.99	5.77E+01	15.19	**
Glycolysis	2,3-BPG	6.12E-01	0.06	3.76E-01	0.09	
	3-phosphoglycerate	3.33E+00	0.48	2.18E+00	0.27	
	acetyl-CoA	6.78E-03	0.00	3.19E-02	0.00	
	dihydroxyacetone phosphate	2.70E-01	0.06	4.02E-01	0.03	
	fructose 1,6-bisphosphate	1.62E-01	0.05	1.22E-01	0.02	
	glucose	1.26E+00	0.16	4.05E+00	1.57	
	glucose 6-phosphate	2.26E-01	0.04	5.57E-01	0.17	
	glyceraldehyde 3-phosphate	4.20E-01	0.10	5.44E-01	0.11	
	lactate	3.41E+00	0.80	9.01E+00	3.33	****
	phosphoenolpyruvate	2.57E+00	0.31	2.20E+00	0.22	
	pyruvate	3.23E-01	0.08	5.09E-01	0.19	
His	carnosine	2.82E-02	0.01	7.23E-02	0.02	
	histidine	7.68E+00	0.82	1.35E+01	3.72	
Ile Leu Val	isoleucine	2.87E+01	3.69	4.96E+01	13.86	
	leucine	2.30E+01	2.20	3.89E+01	11.62	
	valine	2.17E+01	2.40	3.88E+01	10.88	
Lys Degradation	2-aminoadipate	2.20E-01	0.02	2.18E-01	0.08	
	2-oxoadipate	1.48E-01	0.04	1.83E-01	0.04	
	lysine	2.40E+01	3.15	4.52E+01	12.34	**
	Ne-acetyllysine	1.41E+00	0.26	2.61E+00	0.52	
	pipecolic acid	1.59E-02	0.00	1.58E-02	0.00	
	saccharopine	1.22E-03	0.00	5.65E-02	0.02	
One-Carbon	folate	6.28E-02	0.00	3.21E-01	0.00	
Pentose Phosphate Pathway	6-phosphogluconate	1.74E-02	0.01	7.90E-03	0.00	
	erythrose 4-phosphate	8.89E-04	0.00	8.00E-04	0.00	
	ribose ribulose 5-phosphate	1.30E-01	0.02	2.74E-01	0.05	
	sedoheptulose 7-phosphate	1.34E-01	0.02	1.80E-01	0.03	
	UDP-hexose	3.73E+00	0.84	2.52E+00	0.36	*
Phe	N-acetylphenylalanine	0.00E+00	0.00	0.00E+00	0.00	
	phenylacetyl glutamine	1.11E-04	0.00	0.00E+00	0.00	
	phenylalanine	1.29E+01	1.36	2.22E+01	6.06	
Purine	adenine	2.14E-01	0.04	3.98E-01	0.06	
	adenosine	3.93E-01	0.10	6.99E-01	0.16	
	ADP	7.85E-01	0.13	7.11E-01	0.11	
	ADP-ribose	5.89E-03	0.00	1.13E-02	0.00	
	AICAR	1.11E-04	0.00	1.10E-03	0.00	
	AMP	1.10E-01	0.02	1.30E-01	0.02	
	ATP	4.61E+00	0.43	5.00E+00	0.32	
	GAR	0.00E+00	0.00	1.00E-04	0.00	
	GDP	1.10E-01	0.02	7.64E-02	0.01	
	GMP	1.29E-02	0.00	1.17E-02	0.00	
	GTP	3.62E-01	0.04	3.95E-01	0.04	
	guanine	3.33E-04	0.00	8.30E-03	0.00	
	hypoxanthine	3.33E-04	0.00	1.22E-02	0.01	
	IMP	8.78E-03	0.00	3.30E-03	0.00	
	inosine	0.00E+00	0.00	0.00E+00	0.00	
	urate	1.21E-01	0.02	2.50E-02	0.01	
	xanthine	3.57E-02	0.01	4.28E-02	0.02	
Pyrimidine	3-ureidopropionate	4.44E-04	0.00	0.00E+00	0.00	
	beta-alanine	7.47E-01	0.13	1.02E+00	0.18	
	carbamoyl aspartate	1.86E-01	0.03	5.70E-01	0.12	**
	CDP	3.02E-02	0.01	2.20E-02	0.01	
	CMP	6.67E-03	0.00	3.40E-02	0.00	
	CTP	3.35E-01	0.04	3.67E-01	0.06	
	cytosine	2.22E-04	0.00	1.00E-04	0.00	
	dTMP	0.00E+00	0.00	0.00E+00	0.00	
	dTTP	1.04E-02	0.00	1.68E-02	0.00	
	orotate	2.21E-02	0.01	3.58E-02	0.01	
	pseudouridine	1.11E-04	0.00	0.00E+00	0.00	
	UDP	5.09E-01	0.09	4.27E-01	0.08	
	UMP	5.10E-02	0.01	6.67E-02	0.01	
	uracil	7.78E-04	0.00	6.00E-04	0.00	
	UTP	1.48E+00	0.19	1.69E+00	0.23	
Taurine	hypotaurine	4.25E-01	0.10	4.72E-02	0.01	**
	taurine	3.83E-01	0.06	2.51E-01	0.09	
TCA Cycle	2-hydroxyglutarate	3.13E+00	0.36	2.61E+00	0.18	
	acetyl-CoA	6.78E-03	0.00	3.19E-02	0.00	
	alpha-ketoglutarate	2.66E+01	2.03	2.57E+01	0.82	
	cis-aconitrate	3.09E+00	0.81	3.27E+00	0.37	
	citrate	5.03E+01	6.21	5.78E+01	5.47	
	fumarate	1.10E-01	0.02	8.50E-02	0.02	
	GSH	3.34E+00	0.54	4.63E+00	0.63	
	malate	3.08E+01	2.35	3.34E+01	4.34	
	succinate	3.79E-01	0.04	2.72E-01	0.02	
Trp	kynurenine	6.56E-03	0.00	1.44E-02	0.00	
	tryptophan	6.77E-01	0.05	1.07E+00	0.21	*

Significantly Increased (blue)
Significantly Decreased (purple)

Table 1. Whole cell polar metabolomics analysis from CTR and RTT ASTs. CTR n = 9, RTT n = 10. Statistical analysis 2-Way ANOVA with Bonferroni correction. One-Carbon Pathway analyzed by Student T-Test. *$p \leq 0.05$, **$p \leq 0.01$, ***$p \leq 0.001$, ****$p \leq 0.0001$.
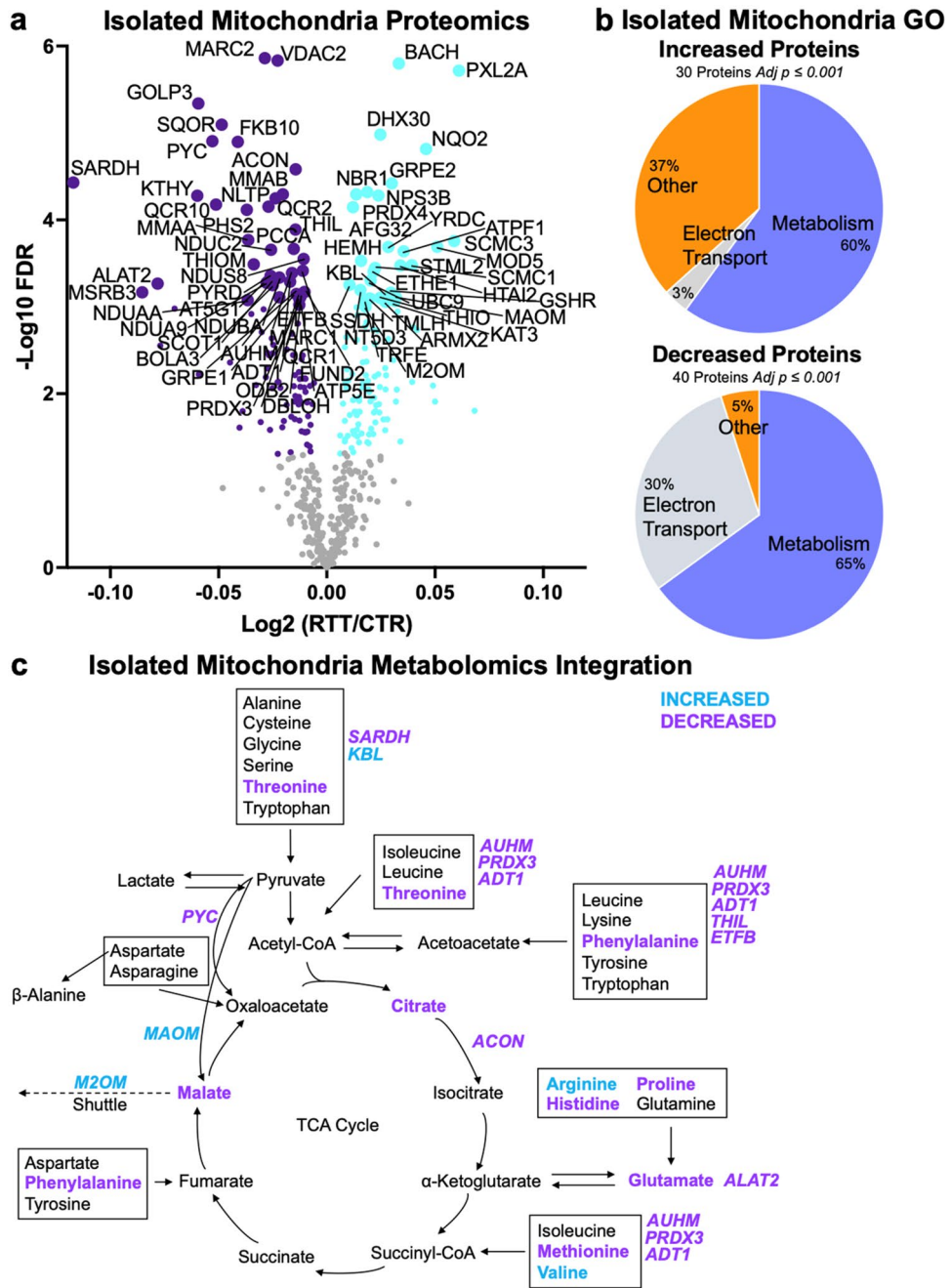
Fig. 6. Integration of metabolomics and proteomics analyses indicates molecular changes tied to mitochondrial dysfunction in RTT AST. (**a**) Volcano plot of AST isolated mitochondria proteomic analysis. Total protein (UniProt) changes of RTT compared to CTR. Increased proteins (light blue), decreased proteins (purple) in RTT compared to CTR. Large dots labeled with adjusted ***$p \leq 0.001$, small dots adjusted *$p \leq 0.05$. CTR n = 6, RTT n = 6. (**b**) Gene ontology (GO) analysis of significantly alter proteins from isolated mitochondria adjusted ***$p \leq 0.001$. Corresponding number of proteins indicated above each pie chart. Gene ontology from MitoCarta[44]. (**c**) Proteomics and metabolomics integration summary from AST isolated mitochondria. TCA cycle with metabolite changes of RTT relative to CTR (significantly increased in blue, significantly decreased in purple). Metabolites in normal font, proteins in italicized font. Metabolomics analysis CTR n = 8, RTT n = 8, Statistical analysis 2-Way ANOVA Bonferroni Correction. Full metabolite changes in Table 2.

CD38/cyclic ADP ribose, connexin 43 gap junctions, tunneling nanotubes (TNTs), dendrites, microvesicles, and free mitochondria by extrusions and internalization[60–62]. We tested how uptake of exogenous mitochondria could impact endogenous mitochondrial function in ASTs. We first isolated mitochondria from ASTs, then seeded

Mitochondria Metabolomics	Metabolite	CTR		RTT		p-value
		Mean	SEM	Mean	SEM	
Acetyl Group	acetylcarnitine	5.00E-04	0.00	1.25E-04	0.00	
	acetylserine	3.13E-03	0.00	1.25E-03	0.00	
	butyryl carnitine	1.25E-04	0.00	0.00E+00	0.00	
	carnitine	5.63E-03	0.00	3.75E-03	0.00	
	propionylcarnitine	1.25E-04	0.00	0.00E+00	0.00	
Ala, Asp, Glu	alanine	4.75E-02	0.01	2.81E-02	0.00	
	asparagine	6.25E-04	0.00	0.00E+00	0.00	
	aspartate	6.36E-02	0.01	5.14E-02	0.01	
	glutamate	5.46E-02	0.01	9.00E-03	0.00	****
	glutamine	1.64E-02	0.00	5.75E-03	0.00	
Arg Biosynthesis	arginine	3.49E-02	0.01	1.05E-02	0.00	****
	argininosuccinate	2.13E-03	0.00	0.00E+00	0.00	
	citrulline	5.00E-03	0.00	1.63E-03	0.00	
	Na-acetylornithine	5.00E-04	0.00	0.00E+00	0.00	
	ornithine	1.00E-03	0.00	7.50E-04	0.00	
Arg Pro	arginine	3.49E-02	0.01	1.05E-02	0.00	
	asparagine	6.25E-04	0.00	0.00E+00	0.00	
	citrulline	5.00E-03	0.00	1.63E-03	0.00	
	creatine	1.63E-02	0.01	1.20E-02	0.00	
	proline	1.78E-01	0.03	5.91E-02	0.01	****
Cofactor/Redox Balance	1-methylnicotinamide	2.70E-01	0.03	5.61E-02	0.01	****
	NAD	2.38E-03	0.00	0.00E+00	0.00	
	nicotinamide	5.09E-02	0.01	9.63E-03	0.00	*
	pantothenic acid	2.06E-02	0.00	6.00E-03	0.00	
	S-adenosylmethionine	3.25E-03	0.00	1.13E-03	0.00	
Cys Met	cystathionine	1.88E-03	0.00	2.00E-03	0.00	
	methionine	2.50E-03	0.00	2.50E-04	0.00	**
	S-adenosylmethionine	3.25E-03	0.00	1.13E-03	0.00	**
Fatty Acid Synthesis	acetylcarnitine	5.00E-04	0.00	1.25E-04	0.00	
	palmitate	3.95E-01	0.11	5.35E-01	0.11	
Gly Ser Thr	acetylserine	3.13E-03	0.00	1.25E-03	0.00	
	glycine	1.50E-03	0.00	0.00E+00	0.00	
	guanidinoacetate	1.25E-04	0.00	0.00E+00	0.00	
	sarcosine	9.50E-03	0.01	1.15E-02	0.01	
	serine	2.63E-03	0.00	6.25E-04	0.00	
	threonine	3.45E-02	0.01	1.28E-02	0.00	***
Glycolysis	2,3-BPG	2.50E-04	0.00	0.00E+00	0.00	
	3-phosphoglycerate	4.75E-03	0.00	6.25E-04	0.00	
	dihydroxyacetone phosphate	2.50E-04	0.00	0.00E+00	0.00	
	F6P/G1P	3.89E-01	0.03	3.47E-01	0.04	
	glucose 6-phosphate	1.69E-02	0.00	6.63E-03	0.00	
	glyceraldehyde 3-phosphate	0.00E+00	0.00	2.50E-04	0.00	
	lactate	1.80E-02	0.00	1.39E-02	0.00	
	phosphoenolpyruvate	7.13E-03	0.00	3.63E-03	0.00	
	pyruvate	5.00E-04	0.00	1.25E-04	0.00	
Glycerophospholipid	choline	3.45E-02	0.01	1.11E-02	0.00	
	glycerol 3-phosphate	0.00E+00	0.00	0.00E+00	0.00	
	glycerophosphocholine	8.23E-02	0.02	1.10E-02	0.00	
	phosphocholine	7.99E-01	0.11	1.34E-01	0.01	****
	phosphoethanolamine	0.00E+00	0.00	0.00E+00	0.00	
His	histidine	1.44E-02	0.00	6.38E-03	0.01	***
	methionine	2.50E-03	0.00	2.50E-04	0.00	
Ile Leu Val	isoleucine	1.78E-02	0.00	4.00E-03	0.00	
	leucine	2.50E-02	0.00	1.20E-02	0.00	
	valine	1.09E-01	0.03	1.59E-01	0.01	*
Ketone Bodies	acetoacetate	1.25E-04	0.00	0.00E+00	0.00	
Lys Degradation	2-aminoadipate	7.85E-01	0.05	7.05E-01	0.05	
	2-oxoadipate	2.45E-01	0.03	1.60E-01	0.02	
	lysine	2.70E-02	0.00	1.05E-02	0.00	
	Na-acetylornithine	5.00E-04	0.00	0.00E+00	0.00	
	pipecolic acid	1.00E-03	0.00	1.00E-03	0.00	
Pentose Phosphate Pathway	6-phosphogluconate	5.88E-03	0.00	6.25E-04	0.00	****
	erythrose 4-phosphate	8.75E-04	0.00	6.25E-04	0.00	
	sedoheptulose 7-phosphate	1.38E-03	0.00	0.00E+00	0.00	
	UDP-hexose	2.38E-03	0.00	0.00E+00	0.00	*
Phe	phenylalanine	1.18E-02	0.00	4.00E-03	0.00	**
Purine	adenine	5.00E-03	0.00	4.63E-03	0.00	
	adenosine	5.75E-03	0.00	7.50E-04	0.00	***
	ADP	9.50E-03	0.00	1.25E-04	0.00	****
	ADP-ribose	1.50E-03	0.00	0.00E+00	0.00	
	AMP	1.75E-03	0.00	0.00E+00	0.00	
	ATP	3.00E-03	0.00	1.25E-04	0.00	
	GDP	1.13E-03	0.00	0.00E+00	0.00	
	GMP	1.25E-04	0.00	0.00E+00	0.00	
	GTP	1.25E-04	0.00	0.00E+00	0.00	
	guanine	1.38E-03	0.00	5.00E-04	0.00	
	hypoxanthine	2.38E-03	0.00	8.75E-04	0.00	
	IMP	9.38E-03	0.00	5.00E-04	0.00	****
	urate	2.50E-04	0.00	0.00E+00	0.00	
	xanthine	1.88E-03	0.00	0.00E+00	0.00	
Pyrimidine	beta-alanine	1.25E-04	0.00	2.50E-04	0.00	
	orotate	1.25E-04	0.00	0.00E+00	0.00	
	UDP	8.75E-04	0.00	0.00E+00	0.00	
	UDP-GlcNAc	8.38E-03	0.00	5.00E-04	0.00	****
	UMP	7.50E-04	0.00	2.50E-04	0.00	
	UTP	2.50E-04	0.00	0.00E+00	0.00	
TCA Cycle	2-hydroxyglutarate	5.31E-02	0.01	3.76E-02	0.00	
	alpha-ketoglutarate	1.04E-01	0.02	4.08E-02	0.00	
	cis-aconitate	2.86E-02	0.00	1.84E-02	0.00	
	citrate	7.06E-01	0.11	4.37E-01	0.10	****
	fumarate	2.86E-02	0.01	1.93E-02	0.00	
	malate	4.94E-01	0.07	1.47E-01	0.01	****
	succinate	9.05E-02	0.01	5.60E-02	0.01	
Significantly Increased						
Significantly Decreased						

Table 2. Isolated mitochondria from CTR and RTT ASTs polar metabolomics analysis. CTR n = 8, RTT n = 8. Statistical analysis 2-Way ANOVA Bonferroni Correction. Ketone bodies and phenylalanine analyzed by Student T-Test. $*p \leq 0.05$, $**p \leq 0.01$, $***p \leq 0.001$, $****p \leq 0.0001$.

Whole Cell Metabolomics	Metabolite	CTR Mean	SEM	CTR GAL Mean	SEM	CTR GAL/CTR p-value	CTR LIP Mean	SEM	CTR LIP/CTR p-value	CTR - PYR Mean	SEM	CTR -PYR/CTR p-value	RTT Mean	SEM	RTT GAL Mean	SEM	RTT GAL/RTT p-value	RTT LIP Mean	SEM	RTT LIP/RTT p-value	RTT - PYR Mean	SEM	RTT -PYR/RTT p-value
Acetyl Group	acetylcarnitine	2.21E-02	0.01	1.38E-03	0.00		1.00E-03	0.00		1.10E-02	0.01		2.79E-02	0.01	2.10E-03	0.00		5.60E-03	0.00		3.13E-02	0.01	
	acetylserine	1.65E-01	0.03	4.69E-02	0.00		5.71E-02	0.00		1.87E-01	0.03		2.44E-01	0.04	4.82E-02	0.00		5.60E-02	0.00		2.54E-01	0.03	
	butyryl carnitine	0.00E+00	0.00	1.25E-04	0.00		2.50E-04	0.00		0.00E+00	0.00		1.00E-04	0.00	0.00E+00	0.00		1.00E-04	0.00		1.00E-04	0.00	
	C5-carnitines	2.50E-04	0.00	7.50E-04	0.00		1.25E-04	0.00		1.38E-03	0.00		1.30E-03	0.00	1.90E-03	0.00		0.00E+00	0.00		1.20E-03	0.00	
	carnitine	2.50E-04	0.00	3.75E-04	0.00		3.75E-04	0.00		2.50E-04	0.00		2.00E-04	0.00	2.00E-04	0.00		5.00E-04	0.00		2.00E-03	0.00	
	GSH	2.93E+00	0.51	2.33E+00	0.52		2.89E+00	0.43		4.17E+00	0.72	****	4.82E+00	0.84	3.48E+00	0.40		3.11E+00	0.26	****	7.70E+00	0.22	****
	N-acetylglutamate	9.13E-03	0.00	2.13E-03	0.00		4.13E-03	0.00		9.13E-03	0.00		8.71E-02	0.05	2.70E-03	0.00		3.20E-03	0.00		1.91E-02	0.01	
	propionylcarnitine	1.00E-03	0.00	8.75E-04	0.00		1.13E-03	0.00		1.13E-03	0.00		1.60E-03	0.00	1.00E-03	0.00		9.00E-04	0.00		1.30E-03	0.00	
Ala Asp Glu	alanine	7.56E+00	0.75	6.07E+00	1.40		5.34E+00	1.34		5.32E+00	0.88		6.94E+00	0.52	8.22E+00	1.22	****	1.02E+01	1.04		1.02E+01	1.04	****
	asparagine	6.46E-02	0.01	6.56E-02	0.02		4.36E-02	0.01		5.81E-02	0.01		1.37E-01	0.02	1.33E-01	0.01		8.25E-02	0.01		1.14E-01	0.01	
	aspartate	1.06E+01	1.73	2.29E+01	2.43	****	3.23E+01	2.30	****	6.85E+00	1.32		5.54E+00	0.14	2.08E+01	2.52	****	3.98E+01	2.77	****	5.01E+00	0.38	
	glutamate	2.87E+01	1.68	2.23E+01	1.67		2.80E+01	2.28		2.71E+01	2.36		2.73E+01	1.30	2.05E+01	1.53	*	2.42E+01	1.18		2.22E+01	0.54	
	glutamine	4.02E+00	0.45	3.78E+00	0.88		3.57E+00	0.51		4.70E+00	1.17		1.26E+01	2.32	6.77E+00	0.52		5.53E+00	0.29	*	9.37E+00	0.37	****
Arg Biosynthesis	arginine	1.50E+01	1.26	1.49E+01	1.55		9.97E+00	1.15		1.42E+01	1.19		3.00E+01	8.65	1.12E+01	1.06	****	1.12E+01	1.02	****	1.61E+01	0.82	****
	argininosuccinate	2.44E-02	0.00	7.88E-03	0.00		5.75E-03	0.00		8.75E-03	0.00		6.00E-02	0.00	1.47E-02	0.00		2.20E-03	0.00		3.75E-02	0.00	
	citrulline	7.13E-03	0.00	1.15E-02	0.01		3.25E-03	0.00		2.25E-03	0.00		4.70E-03	0.00	5.80E-03	0.00		2.20E-03	0.00		4.40E-03	0.00	
	N-acetylglutamate	9.13E-03	0.00	2.13E-03	0.00		4.13E-03	0.00		9.13E-03	0.00		8.71E-02	0.05	2.70E-03	0.00		3.20E-03	0.00		1.91E-02	0.01	
	Na-acetylornithine	5.00E-04	0.00	3.75E-04	0.00		0.00E+00	0.00		5.00E-04	0.00		3.00E-04	0.00	1.20E-03	0.00		0.00E+00	0.00		2.80E-03	0.00	
	ornithine	2.50E-04	0.00	1.25E-04	0.00		1.25E-04	0.00		2.50E-04	0.00		4.00E-04	0.00	1.00E-04	0.00		1.02E-02	0.00		5.00E-04	0.00	
Arg Pro	asparagine	6.46E-02	0.01	6.56E-02	0.02		4.36E-02	0.01		5.81E-02	0.01		1.37E-01	0.02	1.33E-01	0.01		8.25E-02	0.01		1.14E-01	0.01	
	creatine	5.88E-03	0.00	5.00E-03	0.00		6.50E-03	0.00		2.13E-03	0.00		3.35E-01	0.15	7.18E-01	0.33		9.50E-01	0.41		2.98E-01	0.13	
	hydroxyproline	4.79E-02	0.01	3.71E-02	0.01		2.25E-02	0.00		5.58E-02	0.01		2.82E-02	0.00	1.34E-02	0.00		1.02E-02	0.00		2.53E-02	0.00	
	phosphocreatine	6.25E-04	0.00	0.00E+00	0.00		0.00E+00	0.00		2.50E-04	0.00		1.71E-01	0.07	1.37E-01	0.06		2.42E-01	0.10		1.48E-01	0.08	
	proline	5.38E+01	7.82	5.49E+01	6.03		4.63E+01	6.58		5.70E+01	8.30		1.11E+02	16.04	5.62E+01	5.57	****	7.07E+01	8.90	****	1.01E+02	7.96	
Cofactor/Redox Balance	1-methylnicotinamide	6.29E+01	14.63	8.30E+01	18.18		9.01E+01	25.30		4.99E+01	11.92		8.07E+01	17.91	1.55E+02	35.80		1.55E+02	45.58		6.60E+01	14.52	
	acetyl-CoA	3.00E-03	0.00	2.88E-03	0.00		7.50E-04	0.00		1.00E-03	0.00		1.65E-02	0.00	1.50E-02	0.00		1.50E-03	0.00		1.68E-02	0.00	
	alpha-lipoic acid	0.00E+00	0.00	0.00E+00	0.00		0.00E+00	0.00		0.00E+00	0.00		0.00E+00	0.00	0.00E+00	0.00		0.00E+00	0.00		0.00E+00	0.00	
	FAD	0.00E+00	0.00	0.00E+00	0.00		0.00E+00	0.00		0.00E+00	0.00		0.00E+00	0.00	0.00E+00	0.00		0.00E+00	0.00		0.00E+00	0.00	
	GSH	2.93E+00	0.51	2.33E+00	0.52		2.89E+00	0.43		4.17E+00	0.72		4.82E+00	0.84	3.48E+00	0.40		3.11E+00	0.26		7.70E+00	0.22	
	GSSG	2.23E+00	0.19	2.90E+00	0.44		2.77E+00	0.42		2.21E+00	0.34		3.26E+00	0.54	2.89E+00	0.42		2.62E+00	0.37		2.52E+00	0.22	
	NAD	1.79E+00	0.29	1.82E+00	0.30		1.40E+00	0.19		1.60E+00	0.25		2.61E+00	0.22	2.31E+00	0.17		1.52E+00	0.05		2.45E+00	0.19	
	NADH	1.85E-02	0.00	1.88E-03	0.00		4.25E-03	0.00		1.93E-02	0.01		2.45E-02	0.00	7.10E-03	0.00		8.00E-03	0.00		3.04E-02	0.01	
	NADP	2.94E-02	0.01	3.93E-02	0.00		5.43E-02	0.02		2.79E-02	0.01		4.87E-02	0.00	8.20E-02	0.02		2.35E-01	0.02		4.35E-02	0.00	
	NADPH	7.70E-02	0.01	7.78E-02	0.01		9.19E-02	0.01		6.83E-02	0.01		1.33E-01	0.01	1.29E-01	0.01		1.04E-01	0.01		1.33E-01	0.01	
	nicotinamide	2.57E+00	0.23	2.44E+00	0.21		1.65E+00	0.20		2.45E+00	0.21		5.16E+00	1.66	2.12E+00	0.19		1.72E+00	0.20		2.37E+00	0.12	
	nicotinic acid	7.50E-04	0.00	6.25E-04	0.00		1.25E-04	0.00		7.50E-04	0.00		4.00E-04	0.00	4.00E-04	0.00		8.00E-04	0.00		5.00E-04	0.00	
	pantothenic acid	1.46E+01	1.64	1.27E+01	1.23		1.23E+01	1.38		1.36E+01	1.63		2.91E+01	2.66	1.73E+01	1.18		2.03E+01	1.13		2.55E+01	1.99	
	S-adenosylmethionine	1.01E+00	0.12	1.14E+00	0.17		9.15E-01	0.10		8.73E-01	0.13		2.04E+00	0.27	1.56E+00	0.22		1.56E+00	0.16		1.56E+00	0.13	
Cys Met	cystathionine	0.00E+00	0.00	1.25E-04	0.00		7.50E-04	0.00		1.25E-04	0.00		2.00E-04	0.00	1.00E-04	0.00		1.00E-03	0.00		0.00E+00	0.00	
	cystine	7.75E-03	0.00	1.04E-02	0.00		6.25E-03	0.00		9.75E-03	0.00		5.09E-02	0.03	6.70E-03	0.00		6.70E-03	0.00		9.00E-03	0.00	
	GSH	2.93E+00	0.51	2.33E+00	0.52		2.89E+00	0.43		4.17E+00	0.72		4.82E+00	0.84	3.48E+00	0.40		3.11E+00	0.26		7.70E+00	0.22	
	methionine	7.77E+00	0.73	7.35E+00	0.67		4.60E+00	0.48		6.34E+00	0.63		1.48E+01	4.64	5.86E+00	0.49	****	4.49E+00	0.44	****	6.81E+00	0.31	****
	S-adenosylhomocysteine	4.01E-02	0.01	3.41E-02	0.01		5.68E-02	0.01		6.15E-02	0.02		6.60E-02	0.01	4.25E-02	0.01		8.36E-02	0.01		7.94E-02	0.01	
	S-adenosylmethionine	1.01E+00	0.12	1.14E+00	0.17		9.15E-01	0.10		8.73E-01	0.13		2.04E+00	0.27	1.56E+00	0.22		1.56E+00	0.16		1.56E+00	0.13	
Fatty Acid Synthesis	acetylcarnitine	2.21E-02	0.01	1.38E-03	0.00		1.00E-03	0.00		1.10E-02	0.01		2.10E-02	0.01	2.10E-03	0.00	**	5.60E-03	0.00		3.13E-02	0.01	
	palmitate	2.10E-02	0.01	2.16E-02	0.01		2.24E-02	0.00		3.09E-02	0.01		1.26E-02	0.00	1.54E-02	0.00		1.06E-02	0.00		1.43E-02	0.01	
Glycerophospholipid	choline	5.72E+01	18.63	5.14E+01	19.05		3.22E+01	12.00		6.92E+01	25.02		1.05E+02	30.97	4.71E+01	16.67		5.72E+01	15.48		9.69E+01	26.31	
	glycerol 3-phosphate	9.75E-02	0.03	9.38E-03	0.00		5.00E-04	0.00		1.35E-01	0.04		2.73E-02	2.91	1.10E-03	0.00		0.00E+00	0.00		3.86E-02	0.01	
	glycerophosphocholine	5.17E+01	9.71	1.67E+01	3.77		2.72E+00	0.51		5.74E+01	10.50		2.41E+01	2.91	1.73E+01	1.68		2.25E+00	0.31		5.73E+01	1.98	
	phosphocholine	7.58E+02	135.20	5.32E+02	69.29		4.82E+02	92.47	*	8.25E+02	139.59		1.13E+03	113.24	9.41E+02	120.47		9.79E+02	120.54		1.48E+03	153.43	
	phosphoethanolamine	1.50E+00	0.11	1.81E+00	0.06		3.03E+00	0.26		1.17E+00	0.10		1.36E+00	0.03	6.59E+00	0.11		2.44E+00	0.16		8.55E+00	2.01	
Gly Ser Thr	acetylserine	1.65E-01	0.03	4.69E-02	0.00		5.71E-02	0.00		1.87E-01	0.03		2.44E-01	0.04	4.82E-02	0.00		5.60E-02	0.00		2.54E-01	0.03	
	betaine	1.69E-02	0.02	3.29E-02	0.03		9.13E-02	0.07		1.68E-02	0.00		0.00E+00	0.00	0.00E+00	0.00		1.50E-02	0.03		1.36E+00	0.04	
	glycine	2.09E+00	0.24	1.60E+00	0.20		1.42E+00	0.12		1.68E+00	0.16		1.79E+00	0.17	1.06E+00	0.03		1.00E+00	0.03		1.36E+00	0.04	
	guanidinoacetate	2.50E-03	0.00	0.00E+00	0.00		0.00E+00	0.00		0.00E+00	0.00		6.00E-04	0.00	8.00E-04	0.00		0.00E+00	0.00		1.00E-04	0.00	
	phosphoserine	9.43E-02	0.01	1.04E-01	0.04		1.66E-01	0.04		4.21E-02	0.01		1.76E-02	0.00	7.30E-03	0.00		7.60E-03	0.00		5.20E-03	0.00	
	sarcosine	1.46E-02	0.01	7.25E-03	0.00		3.55E-02	0.02		1.73E-02	0.01		2.06E+00	0.57	7.37E-01	0.02		3.14E-02	0.01		1.08E-02	0.01	
	serine	1.58E+00	0.12	1.31E+00	0.09		9.55E-01	0.08		1.40E+00	0.09		2.06E+00	0.57	2.54E+00	0.05		5.01E-03	0.05		1.92E+00	0.03	
	threonine	6.03E+01	6.59	4.82E+01	4.28		3.44E+01	2.34	****	6.58E+01	4.74		6.58E+01	22.11	3.44E+01	2.47	****	2.97E+01	2.46	****	4.96E+01	1.90	****
Glycolysis	2,3-BPG	3.36E-01	0.03	2.50E-01	0.02		2.30E-01	0.03		1.66E-01	0.03		2.89E-01	0.05	1.56E-01	0.02		1.00E-01	0.01		2.32E-01	0.01	
	3-phosphoglycerate	1.83E+00	0.29	8.51E-01	0.05	*	6.81E-01	0.06	**	8.06E-01	0.11	*	1.36E+00	0.18	5.59E-01	0.06		3.78E-01	0.02	**	1.11E+00	0.07	
	acetyl-CoA	3.00E-03	0.00	2.88E-03	0.00		7.50E-04	0.00		1.00E-03	0.00		1.65E-02	0.00	1.50E-02	0.00		1.50E-03	0.00		1.68E-02	0.00	
	dihydroxyacetone phosphate	1.29E-01	0.02	2.88E-03	0.00		7.50E-04	0.00		1.28E-01	0.02		2.19E-01	0.02	0.00E+00	0.00		0.00E+00	0.00		3.37E-01	0.03	
	fructose 1,6-bisphosphate	1.44E-01	0.03	8.40E-02	0.02		2.64E-02	0.01		5.31E-02	0.02		1.06E-01	0.03	7.30E-02	0.02		5.85E-02	0.02		1.51E-01	0.03	
	glucose	1.72E-01	0.25	2.07E-02	0.00		2.17E-02	0.00		1.83E-02	0.00		3.19E+00	0.99	1.67E+00	0.14		1.03E-02	0.00		1.06E+00	0.19	
	glucose 6-phosphate	1.18E-01	0.02	8.46E-01	0.14		1.83E-02	0.00		1.04E-01	0.02		2.94E-01	0.04	7.52E-01	0.09		1.03E-02	0.00		1.95E-01	0.02	
	glyceraldehyde 3-phosphate	1.18E-01	0.03	3.88E-03	0.00		2.88E-03	0.00		1.22E-01	0.03		2.73E-01	0.01	5.50E-03	0.00		4.60E-03	0.00		2.74E-01	0.03	
	lactate	1.69E+02	0.38	2.39E-01	0.07	****	8.82E-01	0.05		1.36E+00	0.28		4.51E+00	0.99	2.71E+00	0.07	****	4.50E-01	0.04	*	2.88E+00	0.37	****
	phosphoenolpyruvate	1.33E+00	0.17	8.99E-01	0.06		8.82E-01	0.05		6.80E-01	0.17		1.31E+00	0.05	5.86E-01	0.09		4.50E-01	0.04		9.52E-01	0.09	
	pyruvate	2.03E-01	0.05	1.62E-01	0.04		7.58E-02	0.02		3.16E-02	0.01		1.74E-01	0.03	7.83E-02	0.01		4.56E-02	0.01		3.47E-02	0.00	
His	carnosine	4.51E-02	0.01	3.01E-02	0.01		1.26E-02	0.00		4.38E-02	0.01		6.14E-02	0.02	3.75E-02	0.01		2.84E-02	0.01		7.14E-02	0.02	
	histidine	8.75E+00	0.91	8.14E+00	0.83		5.05E+00	0.48		8.24E+00	0.69		1.59E+01	4.76	6.67E+00	0.54		5.00E+00	0.46		8.28E+00	0.45	*
Ile Leu Val	isoleucine	3.73E+01	3.20	3.56E+01	3.44		2.33E+01	2.60		3.39E+01	1.72		6.93E+01	24.72	2.64E+01	2.41	**	1.99E+01	2.06	***	3.34E+01	2.30	*
	leucine	2.91E+01	2.57	2.70E+01	2.81		1.85E+01	2.10		2.56E+01	2.86		5.06E+01	14.30	2.07E+01	1.89		1.70E+01	1.68		2.74E+01	1.81	
	valine	2.17E+01	2.02	2.53E+01	2.35		1.75E+01	1.86		2.56E+01	2.21		5.11E+01	15.08	2.00E+01	1.81		1.70E+01	1.56		2.31E+01	1.28	
Lys Degradation	2-aminoadipate	5.06E-01	0.12	6.96E-01	0.23		2.43E-01	0.05		2.06E-01	0.06		4.06E-01	0.21	9.50E-01	0.26		3.36E-01	0.17		3.56E-01	0.14	
	2-oxoadipate	7.03E-02	0.02	2.51E-01	0.13		3.41E-02	0.01		1.75E-02	0.00		1.19E-01	0.04	1.70E-01	0.07		3.02E-02	0.01		2.60E-02	0.01	
	lysine	1.80E+01	2.18	2.88E+01	3.41		1.91E+01	2.45		2.72E+01	2.47		6.10E+01	18.76	2.67E+01	2.50	****	2.14E+01	2.26	****	3.51E+01	1.72	
	Ne-acetyllysine	3.39E-01	0.07	4.99E-01	0.13		4.50E-01	0.15		4.47E-01	0.12		7.39E-01	0.13	1.54E+00	0.30		1.00E+00	0.43		1.15E+00	0.20	
	pipecolic acid	1.51E-02	0.00	1.09E-02	0.00		1.60E-02	0.00		1.54E-02	0.00		7.36E-02	0.02	1.62E-02	0.00		1.08E-02	0.00		1.68E-02	0.00	
	saccharopine	8.75E-04	0.00	8.75E-04	0.00		5.00E-04	0.00		1.25E-04	0.00		5.03E-02	0.02	4.11E-02	0.02		4.45E-02	0.02		2.61E-02	0.01	
One-Carbon	folate	4.76E-02	0.02	7.26E-02	0.00		5.00E-02	0.02		3.36E-01	0.00		5.81E-02	0.00	5.81E-02	0.00							
Pentose Phosphate Pathway	6-phosphogluconate	1.19E-02	0.02	2.42E-01	0.15		1.00E-03	0.00		4.88E-03	0.00		1.40E-02	0.01	6.90E-03	0.01		6.90E-03	0.01		1.95E-02	0.01	
	erythrose 4-phosphate	7.50E-04	0.00	8.75E-04	0.00		1.00E-03	0.00		1.00E-03	0.00		9.00E-04	0.00	9.00E-04	0.00		7.00E-04	0.00		7.00E-04	0.00	
	ribose ribulose 5-phosphate	5.63E-02	0.01	2.88E-02	0.01		1.40E-01	0.03		4.93E-02	0.01		1.55E-01	0.02	2.44E-02	0.00		2.88E-02	0.00		1.52E-01	0.02	
	sedoheptulose 7-phosphate	5.83E-02	0.02	2.14E-01	0.04		1.40E-01	0.03		4.93E-02	0.01		1.02E-01	0.01	3.15E-01	0.08		2.97E-02	0.00		1.52E-01	0.02	
	UDP-hexose	2.18E+00	0.40	1.61E+00	0.29		2.35E+00	0.59		1.92E+00	0.37		1.58E+00	0.17	9.56E-01	0.10	*	2.15E-02	0.01	****	1.32E+00	0.15	
Phe	N-acetylphenylalanine	0.00E+00	0.00	0.00E+00	0.00		0.00E+00	0.00		0.00E+00	0.00		0.00E+00	0.00	0.00E+00	0.00		1.00E-04	0.00		2.00E-04	0.00	
	phenylacetyl glutamine	0.00E+00	0.00	0.00E+00	0.00		0.00E+00	0.00		0.00E+00	0.00		0.00E+00	0.00	0.00E+00	0.00		0.00E+00	0.00		0.00E+00	0.00	
	phenylalanine	1.69E+01	1.59	1.57E+01	1.56		1.02E+01	1.04		1.60E+01	1.26		2.96E+01	8.67	1.26E+01	1.04		1.01E+01	0.96		1.59E+01	0.76	
Purine	adenine	1.69E-01	0.03	2.01E-01	0.04		9.33E-02	0.01		1.76E-01	0.03		2.83E-01	0.03	2.10E-01	0.03		2.22E-01	0.01		2.28E-01	0.02	
	adenosine	2.92E-01	0.08	4.82E-01	0.16		2.73E-01	0.07		2.81E-01	0.08		5.79E-01	0.12	7.04E-01	0.15		4.93E-01	0.07		5.25E-01	0.07	
	ADP	5.51E-01	0.11	8.10E-01	0.16		8.50E-01	0.13		4.22E-01	0.06		4.70E-03	0.00	2.50E-03	0.00		7.98E-01	0.05		4.89E-01	0.07	
	ADP-ribose	4.13E-03	0.00	4.50E-03	0.00		1.00E-03	0.00		3.13E-03	0.00		4.70E-03	0.00	2.50E-03	0.00		3.00E-03	0.00		1.10E-03	0.00	
	AICAR	0.00E+00	0.00	1.50E-03	0.00		1.25E-04	0.00		0.00E+00	0.00		1.00E-03	0.00	1.30E-03	0.00		0.00E+00	0.00		1.00E-03	0.00	
	AMP	6.45E-02	0.02	1.36E-01	0.03		1.44E-01	0.02		5.78E-02	0.01		1.08E-01	0.01	1.59E-01	0.01		1.59E-01	0.01		9.30E-02	0.01	
	ATP	2.81E+00	0.29	3.00E+00	0.28		3.13E+00	0.29		2.25E+00	0.24	****	3.61E+00	0.41	3.77E+00	0.15		4.11E+00	0.19		3.36E+00	0.35	
	GAR	0.00E+00	0.00	0.00E+00	0.00		0.00E+00	0.00		0.00E+00	0.00		8.77E-02	0.02	9.65E-02	0.01		6.98E-02	0.01		6.98E-02	0.01	
	GDP	9.38E-02	0.02	1.28E-01	0.03		1.09E-01	0.02		6.33E-02	0.01		8.00E-03	0.00	9.70E-03	0.00		5.70E-03	0.00		6.30E-03	0.00	
	GMP	9.63E-03	0.00	3.75E-04	0.00		1.51E-02	0.00		6.88E-03	0.00		2.50E-03	0.00	1.00E-03	0.00		5.70E-03	0.00		4.60E-03	0.00	
	GTP	2.61E-01	0.04	2.37E-01	0.03		2.33E-01	0.03		2.07E-01	0.03		3.27E-01	0.01	2.61E-01	0.01		1.93E-01	0.01		2.81E-01	0.02	
	guanine	8.75E-04	0.00	3.75E-04	0.00		1.00E-03	0.00		1.50E-03	0.00		1.06E-03	0.00	1.20E-03	0.00		3.30E-03	0.00		6.30E-03	0.00	
	hypoxanthine	2.50E-04	0.00	0.00E+00	0.00		0.00E+00	0.00		5.00E-04	0.00		6.70E-03	0.00	0.00E+00	0.00		2.00E-04	0.00		8.70E-03	0.00	
	IMP	2.88E-03	0.00	8.88E-03	0.00		7.75E-03	0.00		2.25E-03	0.00		3.50E-03	0.00	1.02E-02	0.00		4.60E-03	0.00		9.00E-03	0.00	
	inosine	0.00E+00	0.00	0.00E+00	0.00		0.00E+00	0.00		0.00E+00	0.00		4.00E-04	0.00	1.00E-04	0.00		0.00E+00	0.00		1.00E-04	0.00	
	urate	1.50E-02	0.02	2.80E-02	0.01		2.21E-02	0.01		1.94E-02	0.01		8.30E-03	0.00	1.05E-02	0.00		4.67E-02	0.01		9.30E-03	0.00	
	xanthine	1.25E-03	0.00	4.50E-03	0.00		2.38E-03	0.00		1.38E-03	0.00		1.16E-02	0.00	9.40E-03	0.00		9.40E-03	0.00		1.00E-03	0.00	
Pyrimidine	3-ureidopropionate	0.00E+00	0.00	0.00E+00	0.00		0.00E+00	0.00		0.00E+00	0.00		0.00E+00	0.00	0.00E+00	0.00		1.00E-04	0.00		1.00E-04	0.00	
	beta-alanine	8.82E-01	0.11	7.57E-01	0.08		6.82E-01	0.09		7.34E-01	0.12		1.71E+00	0.43	9.24E-01	0.08		9.16E-01	0.08		1.13E+00	0.11	****
	carbamoyl aspartate	3.90E-02	0.01	2.84E-02	0.01		2.50E-02	0.01		2.79E-02	0.01		2.58E-01	0.01	2.83E-02	0.01		1.49E-01	0.01		8.74E-02	0.01	
	CDP	3.20E-02	0.01	2.88E-02	0.01		5.05E-02	0.01		4.13E-02	0.00		2.69E-02	0.01	2.83E-02	0.01		2.40E-02	0.00		2.37E-02	0.01	
	CMP	6.63E-03	0.00	1.30E-02	0.00		1.54E-02	0.01		4.13E-03	0.00		4.16E-03	0.00	5.10E-03	0.00		4.10E-03	0.00		3.01E-01	0.03	
	CTP	2.65E-01	0.05	2.43E-01	0.04		2.85E-01	0.04		2.10E-01	0.04		3.36E-01	0.01	2.61E-01	0.01		1.60E-01	0.01		2.27E-01	0.02	
	cytosine	0.00E+00	0.00	1.25E-04	0.00		0.00E+00	0.00		0.00E+00	0.00		1.06E-04	0.00	1.00E-04	0.00		2.00E-04	0.00		1.00E-04	0.00	
	dTMP	2.88E-03	0.00	1.13E-03	0.00		2.50E-04	0.00		2.50E-03	0.00		1.90E-02	0.00	9.00E-04	0.00		9.00E-04	0.00		2.27E-02	0.00	
	orotate	2.10E-02	0.01	1.45E-02	0.00		1.55E-02	0.00		1.61E-02	0.01		2.50E-02	0.01	1.10E-02	0.00		1.10E-02	0.00		2.50E-02	0.00	
	pseudouridine	1.00E-02	0.00	3.49E-01	0.06		5.96E-01	0.11		1.31E-01	0.03		3.81E-01	0.06	4.67E-01	0.10		3.16E-01	0.04		4.36E-01	0.08	
	UDP	4.77E-01	0.09	3.49E-01	0.06		5.96E-01	0.11		1.31E-01	0.03		3.81E-01	0.06	3.18E-01	0.04		2.94E-01	0.03		4.36E-01	0.08	
	UMP	5.09E-02	0.01	6.95E-02	0.02		7.35E-02	0.02		4.38E-02	0.01		4.82E-02	0.01	1.29E-01	0.01		1.87E-02	0.00		2.91E-02	0.00	
	uracil	0.00E+00	0.00	5.00E-04	0.00		5.00E-04	0.00		0.00E+00	0.00		2.00E-04	0.00	1.00E-04	0.00		0.00E+00	0.00		0.00E+00	0.00	
	UTP	1.38E+00	0.17	9.60E-01	0.14	**	4.05E-01	0.06	***	7.31E-01	0.13		9.52E-02	0.01	8.28E-02	0.01		5.43E-02	0.01		1.23E-01	0.02	
Taurine	hypotaurine	7.83E-01	0.13	6.70E-01	0.11		4.00E-01	0.06		7.31E-01	0.13		9.52E-02	0.01	8.28E-02	0.01		5.43E-02	0.01		1.23E-01	0.02	
	taurine	4.11E-01	0.05	2.63E-01	0.05		3.31E-01	0.01		4.91E-01	0.05		1.99E-01	0.02	9.51E-02	0.02		2.63E-02	0.01		2.16E-01	0.03	
TCA Cycle	2-hydroxyglutarate	1.27E+00	0.10	1.49E+00	0.14		1.36E+00	0.11		1.26E+00	0.14		1.60E+00	0.09	1.81E+00	0.15		1.68E+00	0.20		1.53E+00	0.09	
	acetyl-CoA	3.00E-03	0.00	2.88E-03	0.00		7.50E-04	0.00		1.00E-03	0.00		1.65E-02	0.00	1.50E-02	0.00		1.50E-03	0.00		1.68E-02	0.00	
	alpha-ketoglutarate	9.16E+00	0.80	8.12E+00	1.52		7.89E+00	1.34		4.91E+00	0.65		1.32E+01	1.87	7.22E+00	1.17		7.00E+00	1.00		6.69E+00	0.70	
	cis-aconitrate	9.94E-01	0.26	6.47E-01	0.20		4.44E-01	0.19		4.58E-01	0.17		2.50E+00	0.80	7.92E-01	0.22		4.99E-01	0.15		7.13E-01	0.15	
	citrate	2.27E+01	3.81	1.64E+01	4.49		1.55E+01	5.46		1.28E+01	2.88		4.13E+01	7.18	2.67E+01	5.26		1.96E+01	4.30		1.79E+01	2.45	****
	fumarate	9.38E-02	0.02	6.41E-02	0.02		2.71E-01	0.02		4.17E+00	0.72		4.70E-02	0.01	3.48E+00	0.84		3.11E+00	0.26		7.70E+00	0.22	
	GSH	2.93E+00	0.51	2.33E+00	0.52		2.89E+00	0.43		4.17E+00	0.72		4.82E+00	0.84	3.48E+00	0.40		3.11E+00	0.26		7.70E+00	0.22	
	malate	1.01E+01	1.80	3.73E+00	1.78		6.53E+00	1.58		5.60E+00	1.27		1.81E+01	3.00	6.72E+00	1.07	*	1.21E+01	1.93		6.42E+00	1.49	
	succinate	1.58E-01	0.02	2.42E-01	0.07		1.60E-01	0.01		6.78E-02	0.01		1.54E-01	0.03	2.48E-01	0.01		2.63E-02	0.04		6.00E-02	0.01	
Trp	kynurenine	1.14E-02	0.02	1.20E-02	0.01		1.85E-02	0.00		3.95E-02	0.02		4.17E-02	0.02	1.38E-02	0.00		2.63E-02	0.01		6.44E-02	0.01	
	tryptophan	8.95E-01	0.10	7.96E-01	0.08		5.27E-01	0.04		8.70E-01	0.05	*	1.13E+00	0.20	6.72E-01	0.04		5.78E-01	0.06	***	8.58E-01	0.03	

Significantly Increased
Significantly Decreased

Table 3. Whole cell polar metabolomics analysis from CTR and RTT ASTs. CTR n = 8, CTR GAL n = 8, CTR LIP n = 8, CTR –PYR n = 8, RTT n = 10, RTT GAL n = 10, RTT LIP n = 10, RTT -PYR n = 10. Statistical analysis 2-Way ANOVA with Bonferroni correction. One-Carbon Pathway analyzed by Student T-Test. *$p \leq$ 0.05, **$p \leq$ 0.01, ***$p \leq$ 0.001, ****$p \leq$ 0.0001.

mitochondria onto ASTs for 24-h. By Seahorse assay, we found exogenous mitochondria did not impact basal levels of OCR (Fig. 8a). CTR and RTT exogenous mitochondria had similar impacts on OCR in CTR and RTT ASTs, with higher ATP-linked and spare capacity rates compared to no exogenous mitochondria. Additionally, exogenous RTT mitochondria significantly increased maximal OCR in RTT ASTs. We then compared these results to incubation with superoxide scavenger MitoTEMPO for 24-h (Fig. 8b). We identified a similar trend to the exogenous mitochondria, whereby CTR and RTT ASTs displayed higher levels of ATP-linked and spare capacity in the presence of MitoTEMPO compared to DMSO control in a dose dependent manner. We also observed a small shift in basal OCR for RTT with 100 µM MitoTEMPO. These results indicate that exogenous mitochondria alter OCR similar to the effects after incubation with MitoTEMPO. Figure 8c depicts a model
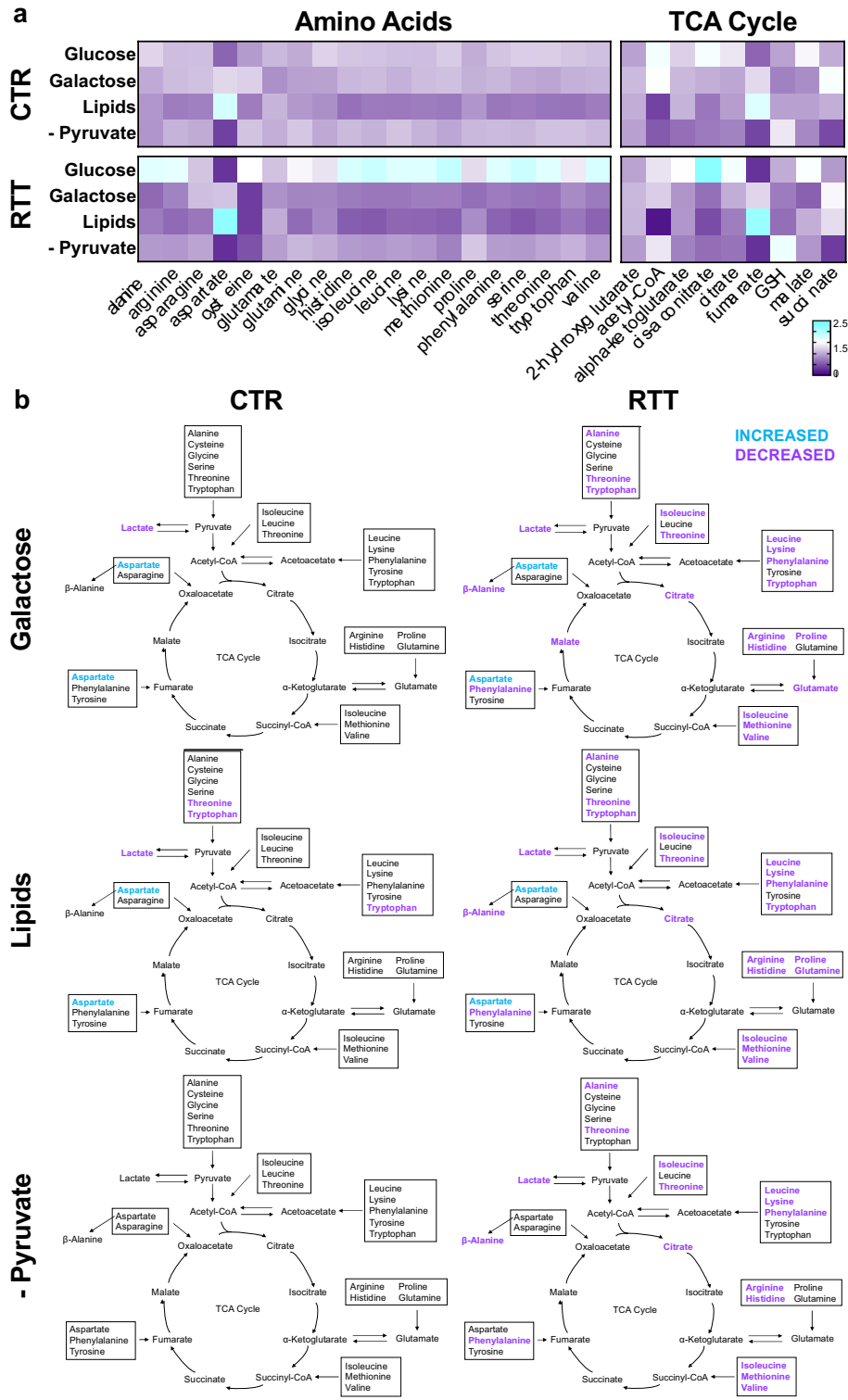
Fig. 7. RTT AST compensate for altered energy demands by catabolizing amino acids. (**a**) Heatmaps of normalized amino acid and TCA cycle metabolites from whole cell AST polar metabolomics. Media exchanged for 24 h, followed by metabolite profiling. Media conditions; Galactose–galactose exchanged for glucose, Lipids–lipid cocktail exchanged for glucose,—Pyruvate–glucose with removal of sodium pyruvate. (**b**) Whole cell AST metabolomics summary. TCA cycle with metabolite changes relative to glucose media control (significantly increased in blue, significantly decreased in purple) in CTR (top panel) and RTT (bottom panel). CTR (Glucose) n = 8, CTR Galactose n = 8, CTR Lipids n = 8, CTR—Pyruvate n = 8, RTT (Glucose) n = 10, RTT Galactose n = 10, RTT Lipids n = 10, RTT—Pyruvate n = 10. Statistical analysis 2-Way ANOVA with Bonferroni correction, $p \leq 0.05$. Full metabolite changes in Table 3.
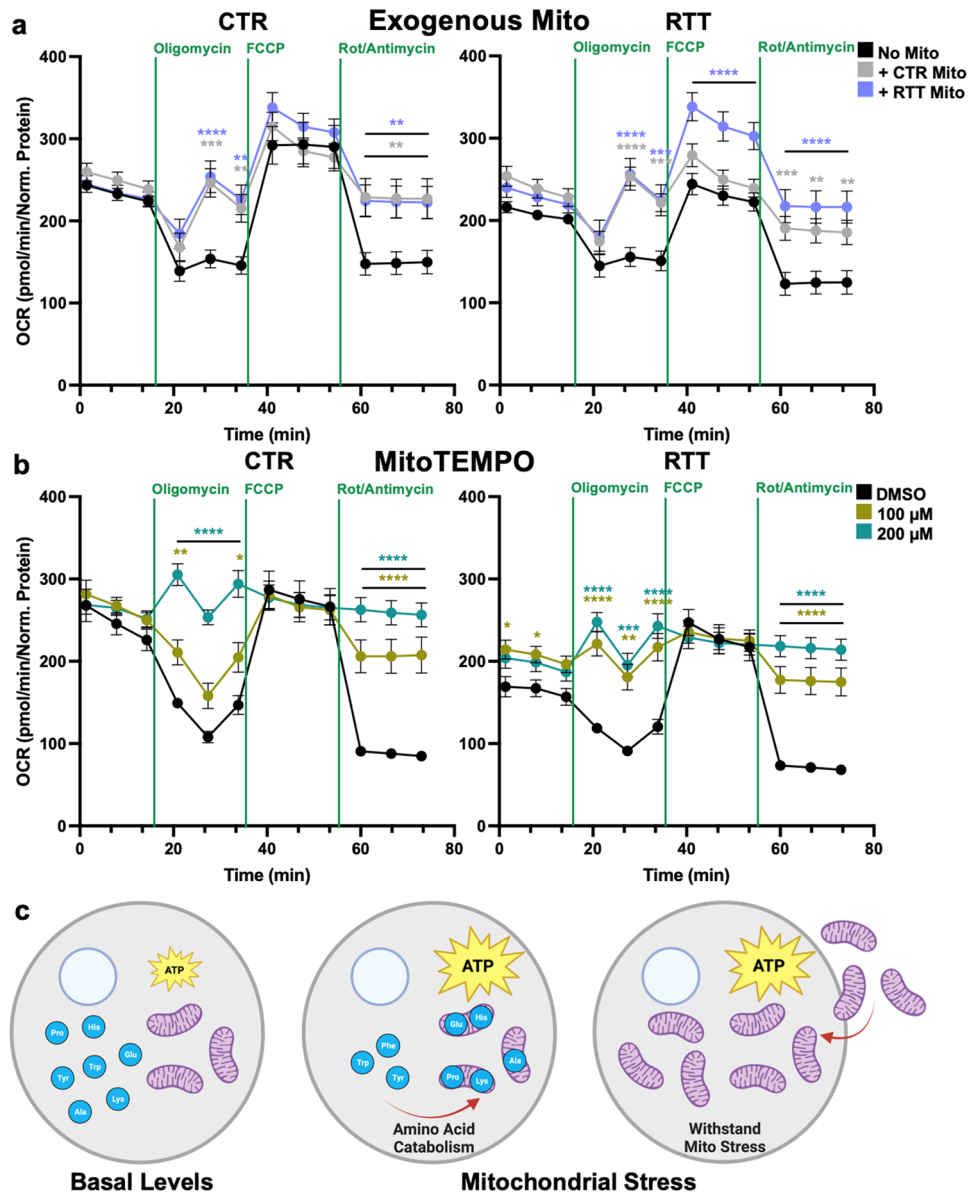
Fig. 8. Exogenous mitochondria improve cellular OCR similar to superoxide scavenger MitoTEMPO in CTR and RTT ASTs. (**a**) Mitochondria stress test of CTR and RTT ASTs after 24 h incubation with exogenous mitochondria from CTR and RTT ASTs. CTR n = 31, CTR + CTR Mito n = 26, CTR + RTT Mito n = 28, RTT n = 33, RTT + CTR Mito n = 28, RTT + RTT Mito n = 26. Statistical analysis Two-Way ANOVA with Bonferroni correction **$p \leq 0.01$, ***$p \leq 0.001$, ****$p \leq 0.0001$. Error bars SEM. (**b**) Mitochondria stress test of CTR and RTT ASTs after 24-h incubation with superoxide scavenger MitoTEMPO. CTR DMSO n = 28, CTR 100 µM n = 32, CTR 200 µM n = 32, RTT DMSO n = 26, RTT 100 µM n = 32, RTT 200 µM n = 32. Statistical analysis Two-Way ANOVA with Bonferroni correction *$p \leq 0.05$, **$p \leq 0.01$, ***$p \leq 0.001$, ****$p \leq 0.0001$. Error bars SEM. (**c**) Model for RTT ASTs. Total ATP levels are decreased and a large abundance of amino acids are present in whole cell RTT AST compared to CTR. Under mitochondrial stress, the pool of amino acids is depleted. Alternatively, RTT ASTs can compensate for mitochondrial stress if exogenous mitochondria are present. Schematics created with BioRender.com.

for RTT ASTs. Under basal conditions, total ATP levels are decreased and a large abundance of amino acids are present in whole cell RTT AST compared to CTR. To compensate for mitochondrial stress, the pool of cytosolic amino acids are depleted. Alternatively, RTT ASTs can compensate for mitochondrial stress if exogenous mitochondria are present. We propose that exogenous mitochondria, even when mitochondria are not at optimal function from RTT ASTs, can enhance overall mitochondria function in ASTs when stressed.

Cortical neurons take up more dysfunctional mitochondria from RTT ASTs, increasing ROS and augmenting LFP activity

Identifying mitochondrial dysfunction in RTT ASTs potentially has an even greater impact on brain development through transfer of mitochondria to neurons. Utilizing an updated method and different lines than our previous report[63], we first examined phenotypic differences between CTR and RTT hESC-derived cortical neurons. We recapitulated the same phenotype that we previously reported, with decreased soma size and less intersections by sholl analysis in RTT compared to CTR neurons[63] (Supplementary Fig. 15a,b). To examine if *MECP2* LOF impacts the ability of ASTs to donate their mitochondria to neurons, and the impact of *MECP2* LOF on the ability of neurons to take up extracellular mitochondria, we examined transcellular mitochondrial movement between ASTs and neurons. Both RTT ASTs and neurons showed the ability to donate and uptake mitochondria, as evidenced by MitoTracker-labeled mitochondria transfer between cell types (Supplementary Fig. 16a–d). Mitochondrial transplantation assays demonstrated that isolated mitochondria from RTT ASTs were taken up by both RTT and CTR neurons, where they potentially fused with endogenous mitochondria (Supplementary Fig. 17a,b). As indicative of MitoTracker positive mitochondria compared to total mitochondria (TOM20), quantitative analysis revealed increased uptake of RTT AST mitochondria by neurons compared to CTRs (Supplementary Fig. 18a,b). Live imaging further supported slow mitochondrial movement from ASTs to neurons, or from exogenously seeded mitochondria into neurons across all genotypes (Supplementary Fig. 19a).

We postulated increased uptake of dysfunctional mitochondria from RTT ASTs could have severe consequences on neuronal function. We tested 3 conditions per cortical neuron genotype, (1) no exogenous AST mitochondria, (2) CTR exogenous AST mitochondria, or (3) RTT exogenous AST mitochondria. First, we seeded mitochondria onto neurons and measured OCR (Supplementary Fig. 19b). Surprisingly, we observed a different impact on mitochondrial function in neurons than ASTs (Fig. 8a). Exogenous mitochondria from CTR and RTT ASTs significantly increased maximal respiration in CTR neurons. The exogenous mitochondria had no significant impact on OCR in RTT neurons. Next, we tested how exogenous AST mitochondria impacted neuronal superoxide abundance. We found increased superoxide abundance in both CTR and RTT neurons exclusively in the presence of RTT AST mitochondria (Fig. 9a). We then examined the impact of CTR or RTT AST mitochondria on neuronal function. We seeded isolated mitochondria from ASTs onto cortical neurons on a multielectrode array plate, where local field potential (LFP) activity was measured over 7 days (Fig. 9b). LFP activity was similar between CTR and RTT neurons over the course of the experiment in the absence of exogenous mitochondria. After addition of exogenous mitochondria isolated from CTR ASTs onto CTR and RTT neurons, we observed relatively no change in activity compared to neurons without mitochondria. However, adding exogenous mitochondria isolated from RTT ASTs onto CTR and RTT neurons resulted in significant changes to LFP activity (Fig. 9b, Table 4). This activity was visualized as roughly six-to-eightfold increase in LFPs for CTR and RTT neurons relative to neurons without exogenous mitochondria. Notably, ATP levels remained unaffected by exogenous RTT mitochondria, suggesting increased ROS leaking from RTT mitochondria impact neuronal activity (Supplementary Fig. 19c). These results underscore the potential pathophysiological consequences of dysfunctional mitochondrial transfer from RTT ASTs to neurons, increasing activity to a hyperexcitable state and highlighting their role in altering neuronal function in a disease context.

Discussion

Together, we define that human RTT ASTs exhibit altered energy metabolism and severe mitochondrial dysfunction. The mechanisms underlying mitochondrial dysfunction in RTT ASTs involved diminished proteins around amino acid metabolism, the TCA cycle, and the ETC. We propose the identification of dysfunctional mitochondria in human RTT ASTs is a significant finding based on the impact of transferred mitochondria to neuronal health and function. This poses further inquiry into non-cell autonomous contribution of ASTs to the development of RTT in the human embryonic brain.

We uncovered a previously unknown mechanism by which mutation of *MECP2* impacts promoter accessibility of nuclear-encoded mitochondrial genes differently in ASTs compared to neurons, which may be one connection to the strong mitochondrial phenotype observed in RTT ASTs. Recent findings have uncovered differences in the nuclear architecture and chromatin organization between different brain cell types that impact transcriptional regulation, and highlights the significant impact MeCP2 plays in transcriptional regulation by modulating active-inactive chromatin[64]. For instance, ASTs in the mouse primary motor cortex showed higher transcriptional activity in a stripe chromosome region compared to intratelencephalic cortical neurons, despite lower transcriptional activity levels in ASTs. Liu and colleagues propose increased physical separation between these regions and the other repressive regions in the chromosome increased the transcriptional activities[64]. While we identified a potential functional mechanism for MECP2 on regulation of nuclear-encoded mitochondrial promoter accessibility in AST, further studies are necessary to discern the MECP2-dependent cause of the mitochondrial alteration in ASTs.

In agreement with other publications examining *MECP2* mutations across species[16], we report that mutation of *MECP2* in human ASTs compromises OxPhos. We observed increased chromatin accessibility and gene expression of nuclear-encoded mitochondrial genes in RTT ASTs and neurons compared to CTR (Fig. 2). However, the mechanism by which these genes are upregulated remains unclear. Kriaucionis and colleagues identified increased expression of ubiquinol-cytochrome c reductase core protein 1 (*Uqcrc1*) in MeCP2-null mouse brains over time, and elucidated that MeCP2 interacts with *Uqcrc1* promoter by chromatin immunoprecipitation[65]. With mitochondrial phenotypes presenting at pre-symptomatic or early symptomatic stages of RTT, Müller and Can previously proposed a progressive decline in mitochondria function[66]. We affirm nuclear-encoded mitochondrial gene expression is altered early in human brain development, impacting mitochondrial function strongly in RTT ASTs. We postulate stressed mitochondria may attempt to improve their functional efficiency
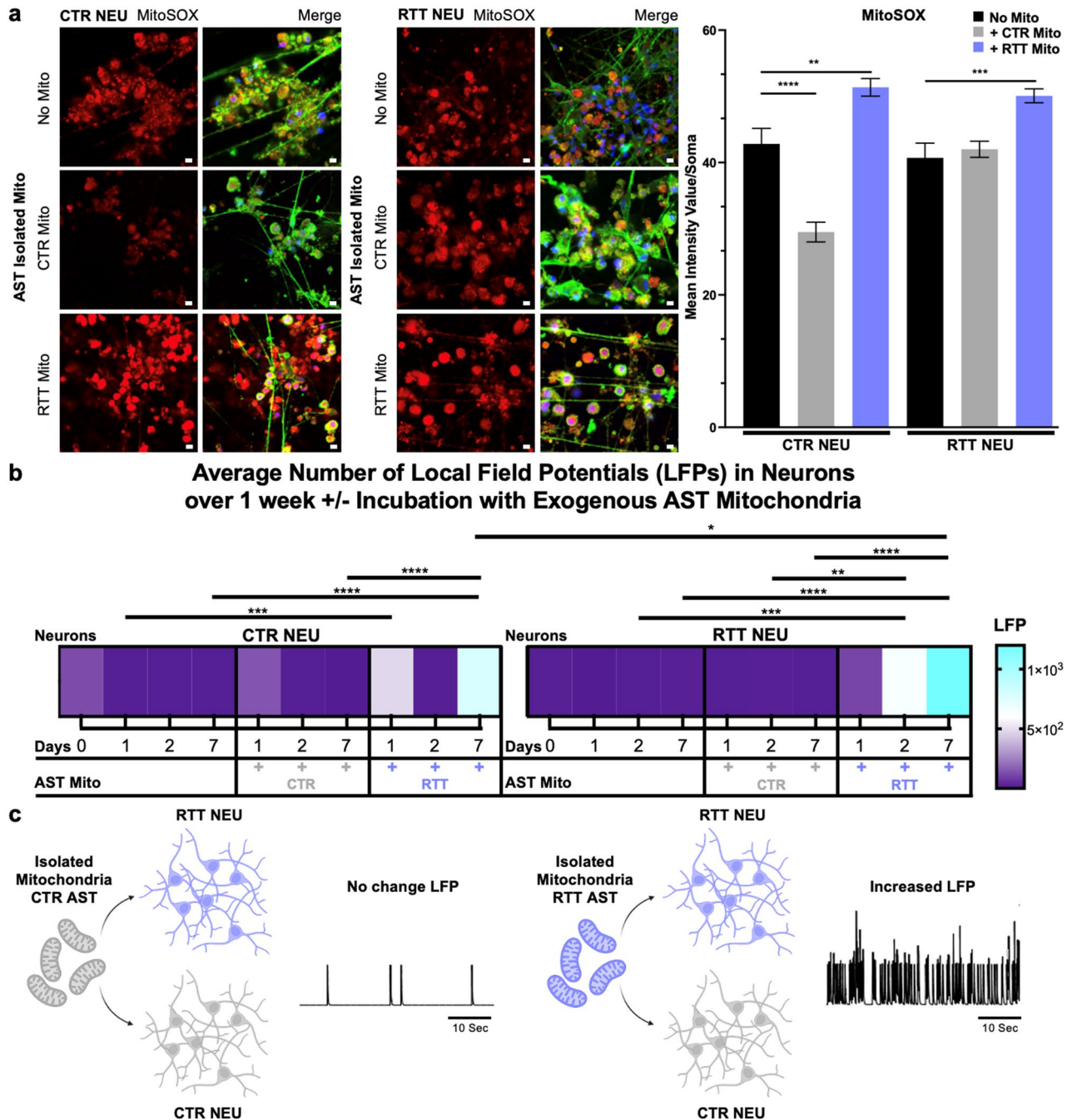
Fig. 9. Dysfunctional mitochondria from RTT ASTs increase neuronal ROS and Local Field Potential (LFP) activity. (**a**) Superoxide abundance in cortical neurons (NEU) after exogenous mitochondrial uptake. Representative images of MitoSOX labeled CTR and RTT cortical NEUs after mitochondrial transplantation. CTR and RTT NEUs have increased superoxide levels with mitochondria isolated from RTT AST compared to NEUs without exogenous mitochondria. Individual soma quantified, CTR NEU n = 26, CTR NEU + CTR Mito n = 44, CTR NEU + RTT Mito n = 95, RTT NEU n = 43, RTT NEU + CTR Mito n = 143, RTT NEU + RTT Mito n = 240. Statistical analysis Two-Way ANOVA with Bonferroni correction **$p ≤ 0.01$, ***$p ≤ 0.001$, ****$p ≤ 0.0001$. Error bars SEM. (**b**) Heatmap of LFPs from Multielectrode Array (MEA) analysis of NEU cultures in absence or presence of exogenous AST mitochondria. Mitochondria were isolated from CTR and RTT AST and seeded onto NEU. LFP activity was measured over 7 days. No conditions are additive. CTR day 0 n = 20, day 1 n = 11, day 2 n = 9, day 7 n = 9, CTR + CTR Mito day 1 n = 5, day 2 n = 4, day 7 n = 5, CTR + RTT Mito day 1 n = 11, day 2 n = 9, day 7 n = 7, RTT day 0 n = 28, day 1 n = 9, day 2 n = 10, day 7 n = 10, RTT + CTR Mito day 1 n = 2, day 2 n = 3, day 7 n = 3, RTT + RTT Mito day 1 n = 14, day 2 n = 14, Day 7 n = 14. Statistical analysis Two-Way ANOVA with Bonferroni correction (Table 4), *$p ≤ 0.05$, **$p ≤ 0.01$, ***$p ≤ 0.001$****$p ≤ 0.0001$. (**c**) Summary of MEA experiment. After addition of mitochondria from CTR ASTs (+ CTR), LFP activity did not significantly differ. After addition of mitochondria from RTT ASTs (+ RTT), LFP activity significantly increased in both CTR and RTT NEUs. Representative LFPs from raster plot of NEUs with CTR or RTT AST mitochondria after 7 days. Schematic created with BioRender.com.

Neuron MEA +/− AST mito	Number of spikes	Mean firing rate (Hz)	Number of bursts	
Day 0 CTR NEU	123.85	0.00	3.70	Mean
	112.55	0.00	3.70	SEM
	20	20	20	n
Day 1 CTR NEU	6.64	0.00	0.00	Mean
	2.69	0.00	0.00	SEM
	11	11	11	n
Day 1 CTR NEU CTR mito	142.80	0.00	0.60	Mean
	137.82	0.00	0.60	SEM
	5	5	5	n
Day 1 CTR NEU RTT mito	477.36	0.02	36.82	Mean
	473.46	0.01	36.82	SEM
	11	11	11	n
Day 2 CTR NEU	3.78	0.00	0.00	Mean
	1.51	0.00	0.00	SEM
	9	9	9	n
Day 2 CTR NEU CTR mito	6.75	0.00	0.00	Mean
	3.77	0.00	0.00	SEM
	4	4	4	n
Day 2 CTR NEU RTT mito	10.33	0.00	0.00	Mean
	7.66	0.00	0.00	SEM
	9	9	9	n
Day 7 CTR NEU	4.44	0.00	0.00	Mean
	2.12	0.00	0.00	SEM
	9	9	9	n
Day 7 CTR NEU CTR mito	1.40	0.00	0.00	Mean
	0.40	0.00	0.00	SEM
	5	5	5	n
Day 7 CTR NEU RTT mito	783.71	0.03	16.00	Mean
	778.72	0.03	16.00	SEM
	7	7	7	n
Day 0 RTT NEU	11.11	0.00	0.00	Mean
	5.35	0.00	0.00	SEM
	28	28	28	n
Day 1 RTT NEU	1.22	0.00	0.00	Mean
	0.15	0.00	0.00	SEM
	9	9	9	n
Day 1 RTT NEU CTR mito	2.00	0.00	0.00	Mean
	1.00	0.00	0.00	SEM
	2	2	2	n
Day 1 RTT NEU RTT Mito	109.29	0.00	0.00	Mean
	46.16	0.00	0.00	SEM
	14	14	14	n
Day 2 RTT NEU	1.90	0.00	0.00	Mean
	0.41	0.00	0.00	SEM
	10	10	10	n
Day 2 RTT NEU CTR mito	14.67	0.00	0.00	Mean
	12.68	0.00	0.00	SEM
	3	3	3	n
Day 2 RTT NEU RTT mito	645.36	0.02	90.21	Mean
	402.95	0.01	89.98	SEM
	14	14	14	n
Day 7 RTT NEU	14.90	0.00	0.00	Mean
	13.79	0.00	0.00	SEM
	10	10	10	n
Continued				

Neuron MEA +/− AST mito	Number of spikes	Mean firing rate (Hz)	Number of bursts	
Day 7 RTT NEU CTR Mito	2.00	0.00	0.00	Mean
	0.58	0.00	0.00	SEM
	3	3	3	n
Day 7 RTT NEU RTT mito	1197.79	0.04	59.43	Mean
	899.30	0.03	55.76	SEM
	14	14	14	n

Table 4. Combined MEA results from Fig. 9b. Statistical analysis 2-Way ANOVA with Bonferroni correction.

to meet homeostatic needs, resulting in increased oxidative stress. The dysfunctional mitochondria may then signal to the nucleus, resulting in a compensatory mechanism by which mitochondrial genes are upregulated.

Müller and Can noted mitochondrial dysfunction in neurons persists for years without causing significant neurodegeneration[63,66]. While neurons largely rely upon OxPhos for ATP generation, ASTs are glycolytic and principally utilize the TCA cycle for biosynthetic processes[45]. Our data indicates that while RTT ASTs show significant mitochondrial dysfunction, neurons appear more resilient, possibly due to their reliance on OxPhos for ATP production. However, increased ROS from RTT AST mitochondria (Figs. 4e, 9a) may cyclically exacerbate mitochondrial dysfunction, further impairing cellular function. Further studies are needed to probe into the MECP2 LOF-dependent impact on mitochondria as progenitor cells differentiation to ASTs and neurons.

In concurrence with the literature[60,62,67], we provide several lines of evidence that mitochondria originating from human ASTs transfer to neurons. We caveat that mitochondrial transfer was observed utilizing live dyes and the quantitative amount of free exogenous mitochondria in proximity to neurons may be extra-physiological. However, our Seahorse analysis indicated that the exogenous mitochondria seeded onto ASTs and neurons did not significantly impact basal levels of OCR (Fig. 8a, Supplementary Fig. 19b). It was only when mitochondria were stressed by the addition of Oligomycin, FCCP, and/or Rot/Antimycin that OCR changed. The increased abundance of mitochondria in ASTs after seeding may buffer the injected drugs, with a lower concentration distributed among the mitochondria. MitoTEMPO did have a small impact on RTT AST basal OCR, suggesting the increased superoxide abundance in RTT mitochondria impacts basal levels of mitochondrial function (Fig. 8b). Further investigations are needed to understand the mechanisms behind these phenotypes. Future studies would benefit from genetically labeled mitochondria in ASTs and neurons in order to track movement during development.

Methods
hESC cell lines and maintenance
hESCs were maintained feeder-free in mTeSR Plus media (STEMCELL Tech 100–0276) on Matrigel coated plates (Corning 354,234) in hypoxic chambers. Passaging of hESC was performed with either ReLeSR (STEMCELL Tech 100–0484) or manual passaging. Mycoplasma contamination was routinely checked for all cells in culture.

Target vector for this knock-in strategy utilized pUC19 plasmid (Addgene) with homology directed repair (Plasmid pCL186_pUC19_HDR_hMECP2-GFP-R168X). Sanger sequencing confirmed that a linker-eGFP transgene was inserted after MECP2-R168 in the Exon 4 position to result in an early truncation (Supplementary Fig. 1a). Western blot confirmed truncated MECP2 with absence of C-terminus (Supplementary Fig. 1b). WIBR3[102] was a generous gift from Dr. Thor Theunissen, Washington University in St. Louis. Unless noted, all experiments used both CTR and RTT lines for analysis.

Stem cell differentiation and maintenance
Astrocytes
Stem cells were transitioned to Glial Progenitor Medium, modified from Muffat et al.[68], containing Neurobasal (Life Technologies 21103049), DMEM/F12/HEPES (Thermo Fisher Scientific 12400024), BSA-v (7.5%) (Gibco 15260-037), GlutaMAX (Life Technologies 35050061), Sodium Pyruvate (Life Technologies 11360070), N-2 (Life Technologies 17502048), 20 ng/mL CNTF (Peprotech AF-450-13-500UG), Penicillin Streptomycin. ASTs were passaged with Accutase (StemCell Technologies 07920), and maturity was confirmed with expression of markers in Supplementary Fig. 11, roughly 150 days from 1st media change.

Astrocyte metabolite media
AST base media. Neurobasal-ᴅ-glucose -sodium pyruvate (Life Technologies A2477501), BSA-v, GlutaMAX, N-2, CNTF, Penicillin Streptomycin. Conditions: *Media*—add 25 mM D-Glucose (Sigma G7021) and sodium pyruvate. *Media + GAL*—add 25 mM D-Galactose (Sigma G0625) and sodium pyruvate. *Media + LIP*—add 1/40 lipid cocktail (gibco 11,905–031) and sodium pyruvate. *Media — PYR*—add 25 mM D-Glucose and same volume of Neurobasal-ᴅ-glucose -sodium pyruvate to exchange sodium pyruvate amount.

Cortical neurons
Neurons were generated according to protocol from Fernandopulle et al.[69]. Briefly, px330-AAVS1-DOX-NGN2-mcherry and px330-guideAAVS1-GFP plasmids were used for gene targeting of NGN2 knock-in at the AAVS1 locus. Lipofectamine Stem Transfection Reagent (Life Technologies STEM00008) and Opti-MEM Reduced

Serum (Life Technologies 31985070) were used for transfection of plasmids into hESC lines. Cells were selected with puromycin, diluted to single cell and screened by expression of mcherry. Multiple clones were expanded and tested for each genotype. After Accutase treatment, 1.5×10^6 cells were seeded in a 6-well plate. After 3 days of Induction Media with Doxycycline, cells were treated with Accutase and seeded onto Matrigel coated plates for final neuron differentiation. Neurons were maintained in BrainPhys Maturation Media, modified from Fernandopulle et al.[69] to include Doxycycline and Culture One supplement (ThermoFisher Scientific, A3320201) to maintain a homogeneous population of cortical neurons. Neurons were matured for at least 2 months for analysis. Axion Biosystems 48-well plates (M768-tMEA-48B), 1×10^5 cells. 96-well imaging plates (ThermoFisher Scientific 165,305) and 96-well Seahorse plates, 1×10^4 cells.

Cerebral organoids

Organoids were constructed with STEMdiff Cerebral Organoid kit (STEMCELL Tech 08570). Organoids were maintained in a normoxic chamber at 37 °C shaking at 100 RPM. After one month from EB seeding, organoids were slowly transferred to maturation media containing Neurobasal, Gem21 (GeminiBio 400–160) Glutamax, and Penicillin Streptomycin. At 5 weeks, organoids were cut at 350 microns to prevent necrotic tissue in the center. Cutting buffer contained HBSS—Ca^{2+} (Life Technologies 14175095) HEPES (Gibco 15630-080) Glucose and Penicillin Streptomycin. Cutting of organoids continued routinely every four weeks until organoid diameter maintained constant size and was no larger than 500 microns. Roughly, organoids were cut 4 times previous to day 100/200 time point for assays with a McIlwain Tissue Chopper at 350 microns.

CLEM

Preparation of organoids for light microscopy

At day 100, organoids were labeled with live dyes. Both dyes were added simultaneously: 0.25 μM NeuO and 200 μM Sulforhodamine 101 (Invitrogen S359) in organoid media for 1 h in incubator shaking. Organoids were washed multiple times, then transferred from culture media and fixed in 4% paraformaldehyde in 0.1 M sodium cacodylate buffer for 1 h at 4 °C. Organoids were rinsed in 0.1 M cacodylate and embedded in warmed 2% low-melting point agar in the cacodylate buffer. Once cooled to 4 °C, 150 μm sections of organoids were prepared by vibratome, and transferred to coverslips. An additional drop of warmed agar was placed on top of the tissue to immobilize sections for handling during light microscopy and processing for resin embedding. Surrounding agar was trimmed to an asymmetrical trapezoid to maintain orientation throughout processing and imaging.

Light microscopy

Light microscopy was performed on a Zeiss LSM 880 Airyscan upright confocal microscope. Sections remained adhered to coverslips during imaging, and were kept wet by adding DI water when needed. Regions of organoid slices were identified with a mix of cell populations and organized morphology using a $40 \times$ water-immersion 1.1NA objective. Z-stacks were collected at 0.1 μm x–y pixel size with 0.54 μm slice spacing, and a subsequent wider 1.5 μm slice spacing to include the tissue margins. Regional z-stacks were acquired by 20×0.8NA objective at 0.15 μm x–y pixel size and 2.2 μm slices, and overview widefield images in transmitted light and fluorescent channels were acquired by 10×0.3NA objective lens. Image conversion and analysis performed with Zen Blue Edition (Zeiss Zen 2.3 zeiss.com/microscopy/us/products/software/zeiss-zen.html).

Tissue processing for electron microscopy

Agar-immobilized organoid sections were post-fixed in 2.5% glutaraldehyde in 0.1 M cacodylate buffer, with special care to keep the exposed side of tissue in contact with solutions. Tissue processing for resin embedding was a variation on a ROTO protocol[70]. In short, samples were further fixed in 1% osmium tetroxide 1.25% potassium ferrocyanide in 0.1 M cacodylate buffer for 1 h at 4 °C, incubated in 1% aqueous thiocarbohydrazide for 20 min at room temperature, and finally fixed in 1% aqueous osmium tetroxide for 1 h at 4 °C. Samples were in bloc stained overnight in 2% uranyl acetate in 0.05 M Maleate buffer. Dehydration was performed in a graded series of ethanol followed by transition into propylene oxide and infiltration into EPON 812 epoxy resin. Slices were oriented in a flat-bottomed mold with tissue facing the block face and embedded in fresh EPON 812. Blocks were polymerized at 60 °C for 48 h.

Ultramicrotomy

Polymerized blocks were trimmed by hand to the extent of the tissue slice, and serial semi thin Sections (0.5 μm) were collected on glass slides, stained with toluidine blue, and observed by light microscopy to locate the region of interest. Locations of nuclei and tissue margins were used to estimate and adjust sectioning orientation and depth with respect to the fluorescent z-stacks. When a semi-thin section contained a portion of the region of interest, 60 nm thin sections were collected on TEM grids. Thin bar hexagonal mesh copper grids coated in a carbon-stabilized nitrocellulose film were used to expose as much of the section area as possible on the grid, while also minimizing section distortions and motions during exposure to the electron beam. After grid collection for STEM imaging, an additional semithin section is collected on a glass slide, coverslipped, and a montage acquired using a $63 \times$ oil-immersion 1.4NA objective as an alignment aid during imaging.

STEM imaging

Electron microscopy was performed on a Zeiss Crossbeam 540 scanning electron microscope equipped with an annular STEM detector. Data was acquired at 30 kV and 362pA probe current, using the ATLAS5 (Zeiss Atlas 5.3.5.3 zeiss.com/microscopy/us/products/software/zeiss-atlas-5.html) automation software. Tissue was located

on the grids at low magnification and 100 nm x–y pixel resolution overview mosaics of the whole tissue region were acquired for each sample condition. Fluorescent, transmitted light, and semithin section data were imported into the ATLAS5 software and co-aligned with the STEM overview data to aid in navigation and correct for compression during sectioning. Regions of interest were identified by intrinsic landmarks within the organoids, and final alignment of the fluorescent z-stacks in 3D was performed through identification of multiple nuclei and cell margins. Using the fluorescent overlay a STEM dataset of 4 nm x–y pixel resolution mosaics comprising the original light microscopy field of view was acquired.

Mitochondrial Quantification
30 images (size 13.5 by 19 μm) were selected per genotype for imaging analysis, where images were selected with clearly defined mitochondria in regions labeled for neurons or glia. Imaging analysis was performed in ImageJ2/Fiji (Version 2.14.0/1.5f. imagej.net) utilizing Region of Interest tools according to Lam et al.[71] *Cells* 2021. Representative measurements are shown in Supplementary Fig. 12.

Multiomics analysis

Organoid preparation and sequencing
At day 100, organoids were flash frozen and stored in − 80 °C. We followed the 10X Genomics Chromium Next GEM Single Cell Multiome ATAC + Gene Expression (1000285) protocol. To provide insight into the specific molecular signatures in a single organoid, we performed the multiomics technique on four individual RTT organoids compared to two individual CTR organoids. Nuclei isolation was followed according to protocol (CG000375 Rev B). Organoids were homogenized with pestle (VWR 47747-358) with 50 strokes and incubated on ice for 5 min. After checking that cells were completely lysed, nuclei were counted with EVE automated cell counter (NanoEnTek). Nuclei were not sorted to maintain integrity. Equal number of nuclei were loaded (4500) according to protocol CG000338 Rev A. Samples were QC with BioAnalyzer, Fragment Analyzer, and qPCR. Libraries were sequenced on a NovaSeq 6000 S2.

Data analysis
We used the 10X Genomics Cell Ranger ARC software v2.0.1, "cellranger-arc mkfastq" to make the fastq files, and "cellranger-arc count" to align the reads, assign them to cells, remove duplicates and count. We used the R packages Seurat[25], version 4.1.1.9001, and Signac[72], version 1.6.0, to process and integrate the multiomics data. We followed the multiomic analysis vignette from Signac (https://stuartlab.org/signac/articles/pbmc_multiomic.html). For each or the six samples we made Seurat objects containing the gene expression data. Chromatin assays, containing the ATAC-seq data, were added to the respective Seurat objects. We merged the four objects into one Seurat object. We calculated the nucleosome signal for each cell barcode, the TSS enrichment score with the "NucleosomeSignal()", and "TSSEnrichment()" functions respectively. We kept cell barcodes that had a nCount_RNA between 2000 and 100,000, a nCount_ATAC between 400 and 600,000, nucleosome signal lower than 2, and a TSS enrichment score higher than 1 and a percentage of RNA-seq reads mapping to genes encoded on the mitochondria lower than 5%. After this filtering we retained 1914 cells from the control 1 organoid, 1722 from the control 2 organoid, 2901 cells from the RTT 1 organoid, 747 cells from the RTT 2 organoid, 177 cells from the RTT 3 organoid, and 179 cells from the RTT 4 organoid. We defined peaks with MACS2 using the ATAC-seq fragments from all the samples. We quantified the fragments overlapping with the peaks, and made a new chromatin assay, "peaks assay" that we used for the ATAC-seq analysis. We integrated the samples on the gene expression assays using cluster similarity spectrum (CSS)[73] implemented in the R package simspec,[73] with 0.05 resolution and following the vignette (github.com/quadbiolab/scRNAseq_analysis_vignette/blob/master/Tutorial.md#step-2-6-data-integration-using-css). We processed and integrated the peaks assay following the scATAC-seq data integration vignette from Signac, (stuartlab.org/signac/articles/integrate_atac.html). Briefly, we used the default Signa implementation of the term frequency-inverse document frequency (TF-IDF) normalization, feature selection and singular value decomposition (SVD) on the TF-IDF matrix. The result of these steps is known as latent semantic indexing (LSI)[72]. We run uniform manifold approximation and projection (UMAP) on the merged Seurat objects using LSI components 2 to 30 as input, since the first LSI component correlated with sequencing depth. To integrate the samples on the peak assays, we selected the integration anchors from peaks that were at 2 Kb or less from a protein coding gene with the "FindIntegrationAnchors" function setting the reduction parameter to "rlsi" and using dimensions 2 to 30. We then integrated the datasets using the "IntegrateEmbeddings" function, with the anchors selected on the previous step, and the 1 to 30 lsi reductions calculated for each sample. We ran UMAP on the resulting integrated LSI using dimensions 1 to 30. Finally, we combined the integrated expression and peak assays via weighted nearest neighbor (WNN) analysis running the function "FindMultiModalNeighbors" on the CCS (from the integrated expression assay) and integrated LSI (from the integrated peaks assay) dimensionality reductions. We ran UMAP and Louvain clustering with 0.05 resolution on the weighted combination of expression and ATAC-seq data. We found 10 clusters. We identified genes specific of each cluster with the "FindAllMarkers" function, selecting only positive markers. To assign cell identities to the clusters, we used the cluster specific markers and the cell-type specific expression analysis tools developed by Camp et al.[26] and Fleck et al.,[27] a human cortex dataset from Nowakowski et al.[28], and the BrainSpan Atlas of the Developing Human Brain[29] via Cell-type Specific Expression Analysis tool developed by Dougherty et al.[30]. Additionally, we assigned cell identity to each cell using a singular value decomposition model implemented with scpred[31] and a developing human cerebral cortex[32] as reference. Briefly, we trained the model on the subset of cells expected to be on the organoids (astrocytes, neurons, neuronal progenitor cells, oligodendrocyte, oligodendrocyte precursor cells and glia). We retrained the model to reclassify NPCs and glial

cells with a mixture discriminant analysis using the R mda package. Lastly, we retrieved the scpred object and used it to predict cell types in our dataset.

We extracted RNA-seq counts or ATAC-seq counts assigned to each gene or promoter for a specific group of cells, converting the Seurat object into a single cell object and exporting the sum of the raw counts overlapping with genes (RNA-seq counts), peaks, or promoters (ATAC-seq counts) for the groups of cells we wanted to compare, e.g., "CTR1" cells or "CTR1 neuronal" cells. We proceeded to analyze these pseudo-bulk counts matrices with DESeq2[74]. In the absence of spike ins, the recommended method for normalizing ATAC-seq data is the use of "full library size factors"[75]. These are normalization factors derived from the total number of fragments in each library, include background reads, and would not be affected by changes in a subset of the opened regions. We normalized our ATAC-seq peaks count matrix using full library size factors as described above. To normalize the pseudo bulk RNA-seq from the single nuclei expression we used the default DESeq2 normalization method. We did not shrink the log2FC of the ATAC-seq peaks analysis. We used normal shrinkage when analyzing the expression data. We ran gene set enrichment analysis with GSEA 4.3.2[76] ranking the genes by the log2 fold change. We used Cluster 3.0[77] the R library heatmap and a custom script to make the heatmap figures.

Immunocytochemistry, immunohistochemistry and microscopy

Astrocytes
For Fig. 4 and Supplementary Figs. 11, 12, ASTs were seeded at a low density (100/well) in 96-well imaging plate. After 24 h, ASTs were washed once in phosphate buffered saline solution (PBS) and fixed in fresh 4% paraformaldehyde (PFA) in PBS for 1 h at room temperature. ASTs were washed multiple times and permeabilized with PBST (1 × PBS solution with 0.1% Triton X-100), then blocked in PBST with 10% BSA for 1 h at room temperature. Primary antibodies (GFAP anti-mouse Dako M0761, NDRG2 abcam ab174850-100μL, EAAT2 anti-mouse Santa Cruz Biotechnology sc-365634, β-actin anti-mouse Proteintech 60008-1-IG, TOM20 anti-rabbit abcam ab186734-100 μL) were added at 1:500 in PBST with 5% BSA overnight at 4 °C. After washing, secondary antibodies (488 anti-mouse Jackson 715-545-151, 594 anti-rabbit Jackson 711-585-152) and DAPI (Life Technologies D1306) were added at 1:1000 in PBST with 5% BSA overnight at 4 °C. After washing, ProLong Diamond Antifade Mountant (Invitrogen P36961) was added to wells prior to imaging. Images were captured on a Zeiss LSM700 confocal microscope and processed with Zen Blue software (Zeiss Zen 2.3) and ImageJ2/Fiji. For imaging-based quantification, unless otherwise specified, at least 12 representative images per genotype/condition were quantified and data were plotted as mean ± SEM with Excel or Graphpad Prism. Full-length western blots are found in Supplementary Fig. 20a.

MitoTracker and MitoSOX assay and analysis
MitoTracker Deep Red (ThermoFisher Scientific, M22426) was diluted to 500 nM in AST media and incubated on ASTs for 1 h in chamber. MitoSOX Red (ThermoFisher Scientific, M36008) was diluted to 5 μM in HBSS + Ca^{2+} and incubated on ASTs for 10 min in chamber. Cells were washed multiple times before fixation. Images were captured on a Zeiss LSM980 airyscan microscope, Z-stacked and processed with Zen Blue and ImageJ2/Fiji. For imaging-based quantification, unless otherwise specified, at least 12 representative images per genotype/condition were quantified and data were plotted as mean ± SEM with Excel or Graphpad Prism.

Mitochondrial transfer between astrocytes and neurons
Cortical neurons were matured for at least 2 months prior to imaging. ASTs or neurons were incubated with MitoTracker Deep Red for 1 h, followed by washing and passaging of ASTs onto neurons at a density of 1×10^4 cells per well. Fixation and antibody protocol is described above. Primary antibodies (MAP2 anti-chicken Encor Biotechnology CPCA-MAP2, GFAP anti-rabbit), secondary antibodies (488 anti-chicken Jackson 703-545-155, 594 anti-rabbit) plus DAPI. For isolated mitochondrial transplantation from ASTs to neurons, isolated mitochondria (see protocol below) were incubated with 1/1000 dilution of 500 nM MitoTracker for 10 min rocking at room temperature. After 48 h, neurons were incubated with MitoSOX for 10 min, then washed multiple times in PBS and fixed with 4% PFA. Primary antibody MAP2 anti-chicken, secondary antibody 488 anti-chicken plus DAPI. Images were captured on a Zeiss LSM700 confocal microscope and processed with Zen Blue software and ImageJ2/Fiji. For imaging-based quantification, unless otherwise specified, at least 12 representative images per genotype/condition were quantified and data were plotted as mean ± SEM with Excel or Graphpad Prism.

Live imaging mitochondrial transfer
Cortical neurons were matured for at least 2 months prior to imaging. Neurons were incubated with 0.25 μM NeuroFluor NeuO (STEMCELL Technologies 01801) for 1 h, and washed 3 times with media. ASTs were incubated with 500 nM MitoTracker Deep Red for 1 h, and washed 4 times prior to passaging with Accutase into neurons at a density of 1×10^4 cells per well. Mitochondria from at least 1.5×10^7 ASTs were isolated, with total protein normalized by Bradford, then incubated with 1/1000 dilution of 500 nM MitoTracker Deep Red for rocking at room temperature 10 min in PBS. Mitochondria were washed 3 times in PBS, resuspended in neuronal media, then seeded onto neurons at 2.5 μg per well. Live imaging was performed on the Nikon Ti automated inverted microscope with incubated chamber at 37 °C and 5% CO$_2$. Recording was performed over 10 h.

Organoids
At day 100 and 200, organoids were washed in PBS and fixed in 4% PFA in PBS. Organoids were preserved and cleared using SHIELD (Lifecanvas technologies C-PCK-250), then permeabilized in PBST and antibodies were added as above. Primary antibodies (1:250) (NeuN anti-mouse EMD Millipore MAB377, GFAP anti-mouse, PSD-95 anti-rabbit abcam ab18258, S100β anti-rabbit Dako Z0311, SYT-1 anti-goat LSBio LS-B5899, MOG

anti-goat LSBio LS-B2419), secondary antibodies (1:500) (488 anti-mouse, 488 anti-goat Jackson 805-545-180, 594 anti-rabbit, 680 anti-goat Jackson 705-625-147, 680 anti-mouse Jackson 715-625-150) plus DAPI (1:1000). Organoids were incubated in EasyIndex optical clearing solution for few hours and mounted on slides in same solution. Images were captured on a Zeiss LSM700 confocal microscope, Z-stacked and processed with Zen Blue software and ImageJ2/Fiji. At least 4 organoids were imaged per condition/genotype.

Mitochondria Isolation

1.5×10^7 cells were collected for mitochondria isolation using kit from ThermoFisher Scientific (89874), with small adjustments to centrifugation times to quickly isolate mitochondria for experimentation. Halt protease Inhibitor cocktail was added to all solutions (Thermo Fisher Scientific 87786). After spinning down for 5 min at 1000 RPM, cells were resuspended in Reagent A and split into two eppendorf tubes. Cells were lysed with pestle (VWR 47747-358) with 50 strokes on ice. After lysis, cells were centrifuged at $700 \times g$ for 5 min, followed by mitochondria collection. Samples were combined, followed by second centrifugation for mitochondria pellet at $3000 \times g$ for 10 min. Mitochondria pellet was washed and spun at $12,000 \times g$ for 5 min. Mitochondria were resuspended in either PBS or Media, followed by Bradford assay to assess total protein. For MEA, mitochondria were seeded at 20 µg per well. For 96-well imaging plates and Seahorse plates, mitochondria were seeded at 2.5 µg per well. Full-length western blots are found in Supplementary Fig. 20b.

qRT-qPCR

Whole cell ASTs (5×10^5 cells) were pelleted and snap frozen, or individual organoids at day 100 were flash frozen. RNA was extracted by RNeasy Plus Micro Kit (Qiagen 74034) and cDNA was synthesized by qScript cDNA Supermix (Quantabio 95048-100). qPCR prepared with Fast SYBR Green Master Mix (appliedbiosystem 2023-08-31) with 384-well plates and run with QuantStudio 6.

qPCR primers	FORWARD	REVERSE
18S	ACCGCAGCTAGGAATAATGGA	GCCTCAGTTCCGAAAACCA
ALDOC	CATTCTGGCTGCGGATGAGTCT	CACACGGTCATCAGCACTGAAC
BLBP/FABP7	CTGTTGTTAGCCTGGATGGAGAC	CTCATAGTGGCGAACAGCAACC
cFOS	GCCTCTCTTACTACCACTCACC	AGATGGCAGTGACCGTGGGAAT
EAAT1	GGTTGCTGCAAGCACTCATCAC	CACGCCATTGTTCTCTTCCAGG
EAAT2	TGCCAACAGAGGACATCAGCCT	CAGCTCAGACTTGGAGAGGTGA
GAPDH	GGAGCGAGATCCCTCCAAAA	GGCTGTTGTCATACTTCTCATGG
GFAP	GAAGCTCCAGGATGAAACCA	ACCTCCTCCTCGTGGATCTT
LDHA	ATGGCAACTCTAAAGGATCAGC	CCAACCCCAACAACTGTAATCT
MAP2	AAACTGCTCTTCCGCTCAGACACC	GTTCACTTGGGCAGGTCTCCACAA
MT-ND1	AAAGGTCCCAACGTTGTAGG	AAGAGCGATGGTGAGAGCTAAG
MT-ND5	TTATATGCTCCGGGTCCATC	AATGGTGAGGGAGGTTGAAG
RBFOX3	TACGCAGCCTACAGATACGCTC	TGGTTCCAATGCTGTAGGTCGC
S100β	GAAGAAATCCGAACTGAAGGAGC	TCCTGGAAGTCACATTCGCCGT
SOX9	AGGAAGCTCGCGGACCAGTAC	GGTGGTCCTTCTTGTGCTGCAC
STAT3	CTTTGAGACCGAGGTGTATCACC	GGTCAGCATGTTGTACCACAGG
TSPO	TCCTACCTGGTCTGGAAAGAGC	CCAGCAGGAGATCCACCAAGG
VIM	TGGACCAGCTAACCAACGAC	GCCAGAGACGCATTGTCAAC

Image analysis

Astrocyte β-actin analysis
Images were converted to 8-bit black and white. Individual ASTs were outlined with the region-of-interest freehand tool in ImageJ2/Fiji.

Neuron characterization
Neuron soma size were measured with straight line freehand tool in ImageJ2/Fiji. Sholl analysis was performed according to ImageJ2/Fiji Sholl Analysis plugin (http://ghoshlab.org/software/ShollAnalysis.pdf).

Mitochondrial quantification
Tom20 and MitoTracker Deep Red labeled mitochondria were analyzed with ImageJ2/Fiji plugin Mitochondria Analyzer for 2D analysis.

Glutamate assay

ASTs were plated at 1×10^5 in 96-well plate. After 48 h, cells were treated with 200 µM GLU for 4 h. Glutamate assay was performed according to protocol with Sigma Glutamate Assay Kit (MAK004).

ATP assay

ASTs were plated at 1×10^5 in 96-well plate. After 48 h, ATP assay was performed according to protocol with abcam ATP Bioluminescence Assay Kit (Ab113849).

Seahorse analysis

ASTs were seeded onto Seahorse Cell Culture 96-well plate at 3×10^4 cells per well, and neurons were seeded at 1×10^4 cells per well. AST basal OCR and ECAR, readings taken 24-h after seeding. For all other experiments, conditions were changed 24-h after AST seeding, and readings taken 24-h after seeding. MitoTEMPO (Millipore-Sigma SML0737) was resuspended in DMSO to final concentration 100 µM or 200 µM. DMSO control volume, 2 µl in 1 mL media (same as 200 µM MitoTEMPO). After 48-h, Seahorse analysis was carried out according to Agilent protocol. Concentrations: Oligomycin 2.5 µM, FCCP 2 µM, Rot/Antimycin 0.5 µM, Glucose 10 mM, Oligomycin in Glycolysis 2.5 µM, 2-DG 50 mM. Reagents: Seahorse XF Cell Mito Stress Test Kit 102,720–100, Seahorse XF Glycolysis Stress Test Kit 103,020–100, Seahorse XF DMEM assay medium pack pH 7.4 103,680–100, Seahorse XFe96 FluxPak mini 102,601–100. After assay, cells were lysed in RIPA buffer followed by Bradford assay to determine total protein levels for normalization. Analysis was performed with Agilent Seahorse Wave software.

Proteomics

Protein extraction, TMT-labelling, solid phase extraction, and peptide fractionation

Isolated ASTs (1×10^6 per sample) or mitochondria (20 µg per sample) samples were lyophilized and resuspended in 23 µL S-trap lysis buffer (5% (w/v) SDS, 50 mM TEAB pH 8.5, 2 mM $MgCl_2$, 10 mM TCEP, 0.025 U/µL Benzonase nuclease), vortexed, and incubated for 10 min at 55 °C. The resulting lysate was centrifuged for 10 min at $20,000 \times g$ and 4 °C and the supernatants were transferred to fresh Eppendorf tubes. Each sample was mixed with 5 µL 500 mM 2-iodoacetamide and the reactions were alkylated at room temperature for 30 min. After that, the protein extracts were acidified with 2.5 µL 27.5% (w/v) phosphoric acid and mixed with 165 µL S-trap binding buffer (100 mM TEAB pH 7.55 in 90% (v/v) ice-cold methanol). All liquid was applied to S-trap Micro columns (ProtiFi CO2-micro) and the protein suspensions were extracted via centrifugation for 1 min at $4000 \times g$. The columns were washed six times with 150 µL S-trap binding buffer and then the columns were placed into fresh Low Protein Binding Microcentrifuge Tubes (Thermo Fisher Scientific 90410). Trapped proteins were cleaved by adding 1 µg trypsin/LysC mix dissolved in 30 µL 50 mM TEAB pH 8.5 and incubating the digests over night at 37 °C in a humified incubator. Tryptic peptides were eluted by centrifuging the columns for 1 min at $4000 \times g$ followed by three washes with 40 µL 50 mM TEAB pH 8.5, 40 µL 0.2% (v/v) formic acid in water, and 40 µL 50% acetonitrile in water, respectively. The collected peptides were lyophilized and resuspended in 20 µL 100 mM TEAB pH 8.5. Peptide concentrations were determined using the Pierce Quantitative Fluorometric Peptide Assay (Thermo Fisher Scientific 23,290) following the descriptions of the manufacturer. Then 2–8 µg peptide was dissolved in 20 µL 100 mM TEAB pH 8.5 and 200 µg TMTpro 16plex labels (Thermo Fisher Scientific A44522) dissolved in 5 µL anhydrous acetonitrile was added to each sample. The labelling reactions were incubated for 60 min at room temperature and subsequently quenched with 2 µL 5% (w/v) hydroxylamine for 30 min. From each labelled stock 10 µL were pooled in a fresh Low Protein Binding Microcentrifuge Tube, respectively. Eluted peptides were lyophilized and reconstituted in 300 µL 0.2% TFA for fractionation using the Pierce High pH Reversed-Phase Peptide Fractionation Kit following the instructions provided by Thermo Fisher Scientific for TMT-labelled samples. The individual peptide fractions were lyophilized and reconstituted in 20 µL 0.2% formic acid in water.

LC–MS

The collection of LC–MS/MS data was conducted using a Vanquish Neo nanoLC equipped with an Orbitrap Eclipse mass spectrometer, a FAIMS Pro Interface, and an Easy Spray ESI source (Thermo Fisher Scientific). An Acclaim PepMap (75 µm × 2 cm) trap column together with a EasySpray ES803 column (75 µm × 50 mm, 100 Å) (both Thermo Fisher Scientific) were employed for nanoLC with 3 µL peptide extract being injected. Peptides were separated using 0.1% (v/v) formic acid in water (solvent A) and 0.1% (v/v) formic acid in 80% (v/v) acetonitrile (solvent B) as mobile phases with a 200 nL/min flow rate and a column temperature of 40 °C. The column was conditioned for two minutes at 5% solvent B and then the linear gradient was gradually increased to up to 40% solvent B over 180 min. Remaining peptides bound to the C18 resin were then eluted for 16 min at 95% B. The ion source temperature was set to a temperature of 300 °C in positive mode at 2100 V and ionized peptides were passed through by the FAIMS Pro unit at − 45, − 55, and − 65 V. The mass spectra were collected with a resolution of 120,000 in DDA (data-dependent acquisition) mode at a mass range of m/z 400–1400, 300% automatic gain control (AGC) target and automatic injection time. The MS/MS fragmentation was performed by picking all precursor ions above 2.0×10^4 intensity at 0.7 Da m/z isolation windows and subjected to high energy collisional dissociation (HCD) using a normalized collision energy of 38. Each precursor ion already collected in MS2 mode was excluded from fragmentation for 60 s. Resulting MS2 product ions were analyzed with a 250% AGC target setting and 200 ms maximum ion accumulation time in the Orbitrap mass analyzer at 50,000 resolutions.

Data analysis

Analysis of proteome raw data files was conducted with the PEAKS X Pro Studio 10.6 (build 20,201,221 bioinfor.com) software package. The data extracted from the .raw files was pre-processed using the following settings: merge scans (10 ppm retention time window; 10 ppm precursor m/z tolerance; precursor mass and charge states z = 2–8) followed by automatic centroiding, deisotoping, and deconvolution. A FASTA database for human

proteins downloaded from Uniprot (UP000005640) or the MitoCarta 3.0 Database[44] was used for protein identification under the following settings: parent mass error tolerance 10 ppm; fragment mass error tolerance 0.05 Da, retention time shift tolerance 5.0 min; semispecific trypsin enzyme specificity; fixed modifications: carbamidomethylation (C), TMTpro; variable modifications: phosphorylation (STY), pyro-glu (Q), oxidation (M), deamidation (NQ); maximal two missed cleavages, maximal three variable posttranslational modifications per peptide. The decoy-fusion approach was utilized to determine the false discovery rates (FDRs) of peptide identifications. Peptide identifications that matched a false discovery rate of ≤ 1% and a significance threshold of 20 (-10lgP) were considered to be identified. The abundance of at least 2 of the most intense peptide signals were utilized to compute the raw protein peak areas. Quantitation of protein was analyzed as described previously[78].

Metabolomics

Whole cell processing
1×10^6 cells per well in 6-well plate, were washed with PBS. Cells were scraped in LC grade methanol and homogenized in Eppendorf tube containing water and LC grade chloroform with pestle mixer, followed by vortexing for 10 min at 4 °C. Polar metabolites were separated by centrifuging top speed at 4 °C. Samples were dried with a nitrogen dryer and stored at − 80 °C until all samples were ready, each sample is biological replicate.

Isolated mitochondria processing
1.5×10^7 cells were spun down for mitochondrial isolation (see protocol below). A small fraction of mitochondria per sample were lysed and tested for protein quantity by Bradford assay. Equal amounts of protein (5 μg) were added to individual eppendorf tubes for metabolite extraction as above. Each sample is technical replicate.

Metabolite profiling
Conducted on a QExactive bench top orbitrap mass spectrometer equipped with an Ion Max source and a HESI II probe, which was coupled to a Dionex UltiMate 3000 HPLC system (Thermo Fisher Scientific). External mass calibration was performed using the standard calibration mixture every 7 days and an additional custom mass calibration was performed weekly alongside standard mass calibrations to calibrate the lower end of the spectrum (m/z 70–1050 positive mode and m/z 60–900 negative mode) using the standard calibration mixtures spiked with glycine (positive mode) and aspartate (negative mode). Typically, samples were reconstituted in 50 uL water and 2 uL were injected onto a SeQuant® ZIC®-pHILIC 150 × 2.1 mm analytical column equipped with a 2.1 × 20 mm guard column (both 5 mm particle size; Millipore-Sigma). Buffer A was 20 mM ammonium carbonate, 0.1% ammonium hydroxide; Buffer B was acetonitrile. The column oven and autosampler tray were held at 25 °C and 4 °C, respectively. The chromatographic gradient was run at a flow rate of 0.150 mL/min as follows: 0–20 min: linear gradient from 80–20% B; 20–20.5 min: linear gradient form 20–80% B; 20.5–28 min: hold at 80% B. The mass spectrometer was operated in full-scan, polarity-switching mode, with the spray voltage set to 3.0 kV, the heated capillary held at 275 °C, and the HESI probe held at 350 °C. The sheath gas flow was set to 40 units, the auxiliary gas flow was set to 15 units, and the sweep gas flow was set to 1 unit. MS data acquisition was performed in a range of m/z = 70–1000, with the resolution set at 70,000, the AGC target at 1×10^6, and the maximum injection time at 20 ms. All solvents, including water, were purchased from Fisher and were Optima LC/MS grade. Relative quantitation of polar metabolites was performed with TraceFinder™ 4.1 (Thermo Fisher Scientific) using a 5 ppm mass tolerance and referencing an in-house library of chemical standards. Data were filtered according to predetermined QC metrics: CV of pools < 25%; R of linear dilution series < 0.975. Metabolite enrichment analysis was performed with www.metaboanalyst.ca.

Western blots

Cells were lysed with pestle (VWR 47747-358) in RIPA buffer (Thermo Fisher Scientific 89900) with Halt Protease Inhibitor Cocktail, and subject to standard immunoblotting analysis. Primary antibodies MECP2 anti-rabbit Invitrogen 49–1029, MECP2 anti-mouse Sigma M7443, TOM20 anti-rabbit, PDI anti-mouse Invitrogen MA3-019, β-actin anti-mouse. Secondary antibodies IRDye 680RD anti-mouse LICOR 926–68,070, IRDye 800CW anti-rabbit LICOR 926–32,211. Note—we changed the fluorescent signal to black and white in LICOR Image Studio (Version 5.5.4 https://www.licor.com/bio/image-studio/). Full-length western blots are found in Supplementary Fig. 20.

Multielectrode array recording

1×10^5 NGN2 hESC were plated and matured at least 2 months in Matrigel plus laminin coated 48-well CytoView plates (Axion Biosystems # M768-tMEA-48B). Recordings of spontaneous activity were taken over 30-min periods on the Maestro system (Axion Biosystems). AxIS software (AxIS 2.4 axionbiosystems.com/products/mea/mea-software) compiled the data collected from recordings. Data were collected for LFPs (firing frequency in Hz), and electrographic burst events (minimum 3 LFPs/100 ms). LFP detection was filtered at 6 × standard deviation to remove potential artifacts. Waveform representative raster plots were obtained through Axion Neural Module software (Neural Metric Tool v1.2.3 axionbiosystems.com/products/mea/mea-software).

Statistical analysis

Statistical parameters including sample sizes and statistical significance are reported in the Figures and the Figure Legends. Data is judged to be statistically significant when $p \leq 0.05$ by two-tailed Student's T-Test, One-way or Two-way ANOVA, where appropriate. Statistical analysis was performed in GraphPad Prism, except for multiomics analysis described above.

Data availability

References

1. Ip, J. P. K., Mellios, N. & Sur, M. Rett syndrome: Insights into genetic, molecular and circuit mechanisms. *Nat. Rev. Neurosci.* **19**, 368–382. https://doi.org/10.1038/s41583-018-0006-3 (2018).
2. Jin, X. R., Chen, X. S. & Xiao, L. MeCP2 deficiency in neuroglia: New progress in the pathogenesis of Rett syndrome. *Front. Mol. Neurosci.* **10**, 316. https://doi.org/10.3389/fnmol.2017.00316 (2017).
3. Sofroniew, M. V. & Vinters, H. V. Astrocytes: Biology and pathology. *Acta Neuropathol.* **119**, 7–35. https://doi.org/10.1007/s00401-009-0619-8 (2010).
4. Okabe, Y. *et al.* Alterations of gene expression and glutamate clearance in astrocytes derived from an MeCP2-null mouse model of Rett syndrome. *PLoS One* **7**, e35354. https://doi.org/10.1371/journal.pone.0035354 (2012).
5. Dong, Q., Kim, J., Nguyen, L., Bu, Q. & Chang, Q. An astrocytic influence on impaired tonic inhibition in hippocampal CA1 pyramidal neurons in a mouse model of rett syndrome. *J. Neurosci.* **40**, 6250–6261. https://doi.org/10.1523/JNEUROSCI.3042-19.2020 (2020).
6. Albizzati, E. *et al.* Identification of region-specific cytoskeletal and molecular alterations in astrocytes of Mecp2 deficient animals. *Front Neurosci* **16**, 823060. https://doi.org/10.3389/fnins.2022.823060 (2022).
7. Williams, E. C. *et al.* Mutant astrocytes differentiated from Rett syndrome patients-specific iPSCs have adverse effects on wild-type neurons. *Hum. Mol. Genet.* **23**, 2968–2980. https://doi.org/10.1093/hmg/ddu008 (2014).
8. Caldwell, A. L. M. *et al.* Aberrant astrocyte protein secretion contributes to altered neuronal development in multiple models of neurodevelopmental disorders. *Nat. Neurosci.* **25**, 1163–1178. https://doi.org/10.1038/s41593-022-01150-1 (2022).
9. Ballas, N., Lioy, D. T., Grunseich, C. & Mandel, G. Non-cell autonomous influence of MeCP2-deficient glia on neuronal dendritic morphology. *Nat. Neurosci.* **12**, 311–317. https://doi.org/10.1038/nn.2275 (2009).
10. Lioy, D. T. *et al.* A role for glia in the progression of Rett's syndrome. *Nature* **475**, 497–500. https://doi.org/10.1038/nature10214 (2011).
11. An, C. *et al.* Overcoming autocrine FGF signaling-induced heterogeneity in naive human ESCs enables modeling of Random X chromosome inactivation. *Cell Stem Cell* **27**, 482–497. https://doi.org/10.1016/j.stem.2020.06.002 (2020).
12. Krishnaraj, R., Ho, G. & Christodoulou, J. RettBASE: Rett syndrome database update. *Hum. Mutat.* **38**, 922–931. https://doi.org/10.1002/humu.23263 (2017).
13. Lengner, C. J. *et al.* Derivation of pre-X inactivation human embryonic stem cells under physiological oxygen concentrations. *Cell* **141**, 872–883. https://doi.org/10.1016/j.cell.2010.04.010 (2010).
14. Zhang, H., Menzies, K. J. & Auwerx, J. The role of mitochondria in stem cell fate and aging. *Development* https://doi.org/10.1242/dev.143420 (2018).
15. de Moura, M. B., dos Santos, L. S. & Van Houten, B. Mitochondrial dysfunction in neurodegenerative diseases and cancer. *Environ. Mol. Mutagen.* **51**, 391–405. https://doi.org/10.1002/em.20575 (2010).
16. Shulyakova, N., Andreazza, A. C., Mills, L. R. & Eubanks, J. H. Mitochondrial dysfunction in the pathogenesis of Rett syndrome: Implications for mitochondria-targeted therapies. *Front. Cell Neurosci.* **11**, 58. https://doi.org/10.3389/fncel.2017.00058 (2017).
17. Gordon, A. *et al.* Long-term maturation of human cortical organoids matches key early postnatal transitions. *Nat. Neurosci.* **24**, 331–342. https://doi.org/10.1038/s41593-021-00802-y (2021).
18. Lewis, J. D. *et al.* Purification, sequence, and cellular localization of a novel chromosomal protein that binds to methylated DNA. *Cell* **69**, 905–914. https://doi.org/10.1016/0092-8674(92)90610-o (1992).
19. Good, K. V., Vincent, J. B. & Ausio, J. MeCP2: The genetic driver of Rett syndrome epigenetics. *Front. Genet.* **12**, 620859. https://doi.org/10.3389/fgene.2021.620859 (2021).
20. Gulmez Karaca, K., Brito, D. V. C. & Oliveira, A. M. M. MeCP2: A critical regulator of chromatin in neurodevelopment and adult brain function. *Int. J. Mol. Sci.* https://doi.org/10.3390/ijms20184577 (2019).
21. Tillotson, R. & Bird, A. The molecular basis of MeCP2 function in the brain. *J. Mol. Biol.* https://doi.org/10.1016/j.jmb.2019.10.004 (2019).
22. Della Ragione, F., Vacca, M., Fioriniello, S., Pepe, G. & D'Esposito, M. MECP2, a multi-talented modulator of chromatin architecture. *Brief Funct. Genomics* **15**, 420–431. https://doi.org/10.1093/bfgp/elw023 (2016).
23. Lee, W., Kim, J., Yun, J. M., Ohn, T. & Gong, Q. MeCP2 regulates gene expression through recognition of H3K27me3. *Nat. Commun.* **11**, 3140. https://doi.org/10.1038/s41467-020-16907-0 (2020).
24. Blondel, V. D., Guillaume, J. L., Lambiotte, R. & Lefebvre, E. Fast unfolding of communities in large networks. *J. Stat. Mech.-Theory E* https://doi.org/10.1088/1742-5468/2008/10/P10008 (2008).
25. Hao, Y. *et al.* Integrated analysis of multimodal single-cell data. *Cell* **184**, 3573–3587. https://doi.org/10.1016/j.cell.2021.04.048 (2021).
26. Camp, J. G. *et al.* Human cerebral organoids recapitulate gene expression programs of fetal neocortex development. *Proc. Natl. Acad. Sci. U. S. A.* **112**, 15672–15677. https://doi.org/10.1073/pnas.1520760112 (2015).
27. Fleck, J. S. *et al.* Inferring and perturbing cell fate regulomes in human brain organoids. *Nature* https://doi.org/10.1038/s41586-022-05279-8 (2022).
28. Nowakowski, T. J. *et al.* Spatiotemporal gene expression trajectories reveal developmental hierarchies of the human cortex. *Science* **358**, 1318–1323. https://doi.org/10.1126/science.aap8809 (2017).
29. Kanton, S. *et al.* Organoid single-cell genomic atlas uncovers human-specific features of brain development. *Nature* **574**, 418–422. https://doi.org/10.1038/s41586-019-1654-9 (2019).
30. Dougherty, J. D., Schmidt, E. F., Nakajima, M. & Heintz, N. Analytical approaches to RNA profiling data for the identification of genes enriched in specific cells. *Nucleic Acids Res.* **38**, 4218–4230. https://doi.org/10.1093/nar/gkq130 (2010).
31. Alquicira-Hernandez, J., Sathe, A., Ji, H. P., Nguyen, Q. & Powell, J. E. scPred: Accurate supervised method for cell-type classification from single-cell RNA-seq data. *Genome Biol.* **20**, 264. https://doi.org/10.1186/s13059-019-1862-5 (2019).
32. Zhu, K. *et al.* Multi-omic profiling of the developing human cerebral cortex at the single-cell level. *Sci. Adv.* **9**, eadg3754. https://doi.org/10.1126/sciadv.adg3754 (2023).
33. Li, W. Excitation and inhibition imbalance in Rett syndrome. *Front. Neurosci.* **16**, 825063. https://doi.org/10.3389/fnins.2022.825063 (2022).
34. Eze, U. C., Bhaduri, A., Haeussler, M., Nowakowski, T. J. & Kriegstein, A. R. Single-cell atlas of early human brain development highlights heterogeneity of human neuroepithelial cells and early radial glia. *Nat. Neurosci.* **24**, 584–594. https://doi.org/10.1038/s41593-020-00794-1 (2021).

35. Cuevas-Diaz Duran, R., Wang, C. Y., Zheng, H., Deneen, B. & Wu, J. Q. Brain region-specific gene signatures revealed by distinct astrocyte subpopulations unveil links to glioma and neurodegenerative diseases. *eNeuro* https://doi.org/10.1523/ENEURO.0288-18.2019 (2019).

36. Nomura, Y. & Segawa, M. Anatomy of Rett syndrome. *Am. J. Med. Genet. Suppl.* **1**, 289–303. https://doi.org/10.1002/ajmg.1320250529 (1986).

37. Yildirim, M. *et al.* Label-free three-photon imaging of intact human cerebral organoids for tracking early events in brain development and deficits in Rett syndrome. *Elife* https://doi.org/10.7554/eLife.78079 (2022).

38. Samarasinghe, R. A. *et al.* Identification of neural oscillations and epileptiform changes in human brain organoids. *Nat. Neurosci.* **24**, 1488–1500. https://doi.org/10.1038/s41593-021-00906-5 (2021).

39. Sun, Y. *et al.* Loss of MeCP2 in immature neurons leads to impaired network integration. *Hum. Mol. Genet.* **28**, 245–257. https://doi.org/10.1093/hmg/ddy338 (2019).

40. Smrt, R. D. *et al.* Mecp2 deficiency leads to delayed maturation and altered gene expression in hippocampal neurons. *Neurobiol. Dis.* **27**, 77–89. https://doi.org/10.1016/j.nbd.2007.04.005 (2007).

41. Mellios, N. *et al.* MeCP2-regulated miRNAs control early human neurogenesis through differential effects on ERK and AKT signaling. *Mol. Psychiatry* **23**, 1051–1065. https://doi.org/10.1038/mp.2017.86 (2018).

42. Morelli, K. H. *et al.* MECP2-related pathways are dysregulated in a cortical organoid model of myotonic dystrophy. *Sci. Transl. Med.* **14**, eabn2375. https://doi.org/10.1126/scitranslmed.abn2375 (2022).

43. Gomes, A. R. *et al.* Modeling Rett syndrome with human patient-specific forebrain organoids. *Front. Cell Dev. Biol.* **8**, 610427. https://doi.org/10.3389/fcell.2020.610427 (2020).

44. Rath, S. *et al.* MitoCarta3.0: An updated mitochondrial proteome now with sub-organelle localization and pathway annotations. *Nucleic Acids Res.* **49**, D1541–D1547. https://doi.org/10.1093/nar/gkaa1011 (2021).

45. Rose, J., Brian, C., Pappa, A., Panayiotidis, M. I. & Franco, R. Mitochondrial metabolism in astrocytes regulates brain bioenergetics, neurotransmission and redox balance. *Front. Neurosci.* **14**, 536682. https://doi.org/10.3389/fnins.2020.536682 (2020).

46. Escartin, C. *et al.* Reactive astrocyte nomenclature, definitions, and future directions. *Nat. Neurosci.* **24**, 312–325. https://doi.org/10.1038/s41593-020-00783-4 (2021).

47. Schousboe, A., Scafidi, S., Bak, L. K., Waagepetersen, H. S. & McKenna, M. C. Glutamate metabolism in the brain focusing on astrocytes. *Adv. Neurobiol.* **11**, 13–30. https://doi.org/10.1007/978-3-319-08894-5_2 (2014).

48. Azarias, G. *et al.* Glutamate transport decreases mitochondrial pH and modulates oxidative metabolism in astrocytes. *J. Neurosci.* **31**, 3550–3559. https://doi.org/10.1523/JNEUROSCI.4378-10.2011 (2011).

49. Sun, J. *et al.* Mutations in the transcriptional regulator MeCP2 severely impact key cellular and molecular signatures of human astrocytes during maturation. *Cell Rep* **42**, 111942. https://doi.org/10.1016/j.celrep.2022.111942 (2023).

50. Esparham, A. E. *et al.* Nutritional and metabolic biomarkers in autism spectrum disorders: An exploratory study. *Integr. Med. (Encinitas)* **14**, 40–53 (2015).

51. Frye, R. E. *et al.* Emerging biomarkers in autism spectrum disorder: A systematic review. *Ann. Transl. Med.* **7**, 792. https://doi.org/10.21037/atm.2019.11.53 (2019).

52. Chen, W. W., Freinkman, E., Wang, T., Birsoy, K. & Sabatini, D. M. Absolute quantification of matrix metabolites reveals the dynamics of mitochondrial metabolism. *Cell* **166**, 1324–1337. https://doi.org/10.1016/j.cell.2016.07.040 (2016).

53. Marroquin, L. D., Hynes, J., Dykens, J. A., Jamieson, J. D. & Will, Y. Circumventing the Crabtree effect: Replacing media glucose with galactose increases susceptibility of HepG2 cells to mitochondrial toxicants. *Toxicol. Sci.* **97**, 539–547. https://doi.org/10.1093/toxsci/kfm052 (2007).

54. Dykens, J. A. *et al.* In vitro assessment of mitochondrial dysfunction and cytotoxicity of nefazodone, trazodone, and buspirone. *Toxicol. Sci.* **103**, 335–345. https://doi.org/10.1093/toxsci/kfn056 (2008).

55. Dott, W., Mistry, P., Wright, J., Cain, K. & Herbert, K. E. Modulation of mitochondrial bioenergetics in a skeletal muscle cell line model of mitochondrial toxicity. *Redox Biol.* **2**, 224–233. https://doi.org/10.1016/j.redox.2013.12.028 (2014).

56. Aguer, C. *et al.* Galactose enhances oxidative metabolism and reveals mitochondrial dysfunction in human primary muscle cells. *PLoS One* **6**, e28536. https://doi.org/10.1371/journal.pone.0028536 (2011).

57. Moczulski, D., Majak, I. & Mamczur, D. An overview of beta-oxidation disorders. *Postepy Hig. Med. Dosw. (Online)* **63**, 266–277 (2009).

58. Yako, H. *et al.* Role of pyruvate in maintaining cell viability and energy production under high-glucose conditions. *Sci. Rep.* **11**, 18910. https://doi.org/10.1038/s41598-021-98082-w (2021).

59. Davis, C. H. *et al.* Transcellular degradation of axonal mitochondria. *Proc. Natl. Acad. Sci. U. S. A.* **111**, 9633–9638. https://doi.org/10.1073/pnas.1404651111 (2014).

60. Hayakawa, K. *et al.* Transfer of mitochondria from astrocytes to neurons after stroke. *Nature* **535**, 551–555. https://doi.org/10.1038/nature18928 (2016).

61. Lampinen, R. *et al.* Neuron-astrocyte transmitophagy is altered in Alzheimer's disease. *Neurobiol. Dis.* **170**, 105753. https://doi.org/10.1016/j.nbd.2022.105753 (2022).

62. Gao, L., Zhang, Z., Lu, J. & Pei, G. Mitochondria are dynamically transferring between human neural cells and alexander disease-associated GFAP mutations impair the astrocytic transfer. *Front. Cell Neurosci.* **13**, 316. https://doi.org/10.3389/fncel.2019.00316 (2019).

63. Li, Y. *et al.* Global transcriptional and translational repression in human-embryonic-stem-cell-derived Rett syndrome neurons. *Cell Stem Cell* **13**, 446–458. https://doi.org/10.1016/j.stem.2013.09.001 (2013).

64. Liu, S. *et al.* Cell-type-specific 3D-genome organization and transcription regulation in the brain. *bioRxiv* https://doi.org/10.1101/2023.12.04.570024 (2023).

65. Kriaucionis, S. *et al*. Gene expression analysis exposes mitochondrial abnormalities in a mouse model of Rett syndrome. *Mol Cell Biol* **26**, 5033–5042 (2006). https://doi.org/10.1128/MCB.01665-05

66. Muller, M. & Can, K. Aberrant redox homoeostasis and mitochondrial dysfunction in Rett syndrome. *Biochem. Soc. Trans.* **42**, 959–964. https://doi.org/10.1042/BST20140071 (2014).

67. Jung, J. E. *et al.* The mitochondria-derived peptide humanin improves recovery from intracerebral hemorrhage: Implication of mitochondria transfer and microglia phenotype change. *J. Neurosci.* **40**, 2154–2165. https://doi.org/10.1523/JNEUROSCI.2212-19.2020 (2020).

68. Muffat, J. *et al.* Human induced pluripotent stem cell-derived glial cells and neural progenitors display divergent responses to Zika and dengue infections. *Proc. Natl. Acad. Sci. U. S. A.* **115**, 7117–7122. https://doi.org/10.1073/pnas.1719266115 (2018).

69. Fernandopulle, M. S. *et al.* Transcription factor-mediated differentiation of human iPSCs into neurons. *Curr. Protoc. Cell Biol.* **79**, e51. https://doi.org/10.1002/cpcb.51 (2018).

70. Tapia, J. C. *et al.* High-contrast en bloc staining of neuronal tissue for field emission scanning electron microscopy. *Nat. Protoc.* **7**, 193–206. https://doi.org/10.1038/nprot.2011.439 (2012).

71. Lam, J. *et al.* A universal approach to analyzing transmission electron microscopy with ImageJ. *Cells* https://doi.org/10.3390/cells10092177 (2021).

72. Stuart, T., Srivastava, A., Madad, S., Lareau, C. A. & Satija, R. Single-cell chromatin state analysis with signac. *Nat. Methods* **18**, 1333–1341. https://doi.org/10.1038/s41592-021-01282-5 (2021).

73. He, Z., Brazovskaja, A., Ebert, S., Camp, J. G. & Treutlein, B. CSS: Cluster similarity spectrum integration of single-cell genomics data. *Genome Biol.* **21**, 224. https://doi.org/10.1186/s13059-020-02147-4 (2020).
74. Love, M. I., Huber, W. & Anders, S. Moderated estimation of fold change and dispersion for RNA-seq data with DESeq2. *Genome Biol.* **15**, 550. https://doi.org/10.1186/s13059-014-0550-8 (2014).
75. Stark R. & Brown G. D. DiffBind: Differential Binding Analysis of ChIP-Seq Peak Data. Bioconductor. Available online at: http://bioconductor.org/packages/release/bioc/html/DiffBind.html (2011).
76. Subramanian, A. *et al.* Gene set enrichment analysis: A knowledge-based approach for interpreting genome-wide expression profiles. *Proc. Natl. Acad. Sci. U. S. A.* **102**, 15545–15550. https://doi.org/10.1073/pnas.0506580102 (2005).
77. de Hoon, M. J., Imoto, S., Nolan, J. & Miyano, S. Open source clustering software. *Bioinformatics* **20**, 1453–1454. https://doi.org/10.1093/bioinformatics/bth078 (2004).
78. Schulte, F., Hasturk, H. & Hardt, M. Mapping relative differences in human salivary gland secretions by dried saliva spot sampling and nanoLC-MS/MS. *Proteomics* **19**, e1900023. https://doi.org/10.1002/pmic.201900023 (2019).

Acknowledgements

Author contributions

D.L.T. and R.J. designed the study and wrote the manuscript. M.I.B. performed multiomics analysis. D.M. and A.L.-J. devised and performed CLEM imaging. K.I.A. assisted in qPCR studies, sholl and mitochondrial analysis. X.S.L. generated the WIBR1R168X hESC line. All other experiments and analyses were performed by D.L.T.

Funding

Competing interests

The authors declare no competing interests.

Additional information

Supplementary Information The online version contains supplementary material available at https://doi.org/10.1038/s41598-024-71040-y.

Correspondence and requests for materials should be addressed to R.J.

Reprints and permissions information is available at www.nature.com/reprints.

Publisher's note Springer Nature remains neutral with regard to jurisdictional claims in published maps and institutional affiliations.